The Regional Influence of an Intense Sierra Barrier Jet and Landfalling Atmospheric River on Orographic Precipitation in Northern California: A Case Study

PAUL J. NEIMAN

Physical Sciences Division, NOAA/Earth System Research Laboratory, Boulder, Colorado

F. MARTIN RALPH

Scripps Institution of Oceanography, University of California, San Diego, La Jolla, California

BENJAMIN J. MOORE

NOAA/ESRL, and Cooperative Institute for Research in the Environmental Sciences, Boulder, Colorado, and Department of Atmospheric and Environmental Sciences, University at Albany, State University of New York, Albany, New York

ROBERT J. ZAMORA

Physical Sciences Division, NOAA/ESRL, Boulder, Colorado

(Manuscript received 7 November 2013, in final form 27 February 2014)

ABSTRACT

A 915-MHz wind profiler, a GPS receiver, and surface meteorological sites in and near California's northern Central Valley (CV) provide the observational anchor for a case study on 23–25 October 2010. The study highlights key orographic influences on precipitation distributions and intensities across northern California during a landfalling atmospheric river (AR) and an associated Sierra barrier jet (SBJ). A detailed wind profiler/GPS analysis documents an intense AR overriding a shallow SBJ at ~750 m MSL, resulting in record early season precipitation. The SBJ diverts shallow, pre-cold-frontal, incoming water vapor within the AR poleward from the San Francisco Bay gap to the northern CV. The SBJ ultimately decays following the passage of the AR and trailing polar cold front aloft. A statistical analysis of orographic forcing reveals that both the AR and SBJ are crucial factors in determining the amount and spatial distribution of precipitation in the northern Sierra Nevada and in the Shasta–Trinity region at the northern terminus of the CV. As the AR and SBJ flow ascends the steep and tall terrain of the northern Sierra and Shasta–Trinity region, respectively, the precipitation becomes enhanced. Vertical profiles of the linear correlation coefficient quantify the orographic linkage between hourly upslope water vapor flux profiles and hourly rain rate. The altitude of maximum correlation (i.e., orographic controlling layer) is lower for the shallow SBJ than for the deeper AR (i.e., 0.90 versus 1.15 km MSL, respectively). This case study expands the understanding of orographic precipitation enhancement from coastal California to its interior. It also quantifies the connection between dry antecedent soils and reduced flood potential.

1. Introduction

The hydrometeorology in the northern half of California's Central Valley (CV) and the adjacent Sierra Nevada and Mt. Shasta–Trinity Alps region (see Fig. 1) has received considerable attention over the last decade through ongoing field campaigns associated with the National Oceanic and Atmospheric Administration's (NOAA) Hydrometeorological Testbed (HMT) program (Ralph et al. 2005a, 2013a; White et al. 2012) and the California Energy Commission's CalWater project (www.esrl.noaa.gov/psd/calwater). The motivation for this attention has been driven largely by water supply and hydroelectric issues and flood-control concerns affecting a majority of the state's ~38 million residents, since much of the region's snowmelt and rainfall collect in expansive reservoirs behind large dams. This

Corresponding author address: Paul J. Neiman, NOAA/Earth System Research Laboratory/Physical Sciences Division, Mail Code R/PSD2, 325 Broadway, Boulder, CO 80305.
E-mail: paul.j.neiman@noaa.gov

DOI: 10.1175/JHM-D-13-0183.1

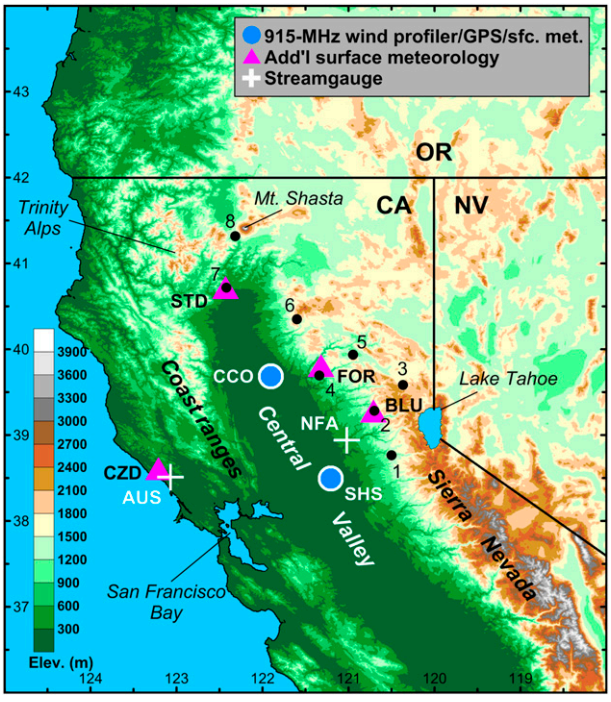

FIG. 1. Terrain base map of northern California, southern Oregon, and western Nevada showing the locations of two 915-MHz wind profilers (CCO and SHS, blue circles), four surface meteorological stations (FOR, STD, BLU, and CZD, pink triangles; BLU and CZD also include soil moisture probes), two stream gauges (NFA and AUS, white pluses), and the eight precipitation gauges that comprise the northern Sierra eight-station precipitation index (black dots labeled 1–8; see Table 1 to cross reference these numbers). The domain is shown as the blue rectangle in Fig. 2a.

precipitation can be heavy in the mountains because of orographic enhancement during the landfall of winter storms (e.g., Heggli and Rauber 1988; Pandey et al. 1999; Dettinger et al. 2004; Galewsky and Sobel 2005; Reeves et al. 2008; Smith et al. 2010). In addition to providing valuable water resources across California (e.g., Dettinger et al. 2011), the heavy precipitation subjects vulnerable population centers to the threat of major flooding (e.g., Dettinger et al. 2012), including the state capital of Sacramento, which is recognized as one of the most vulnerable cities in the United States to the ravages of catastrophic flooding (Lund et al. 2007).

Two atmospheric phenomena significantly modulate the distribution of precipitation, high-altitude snowpack, and runoff in the mountains surrounding California's northern CV: terrain-locked Sierra barrier jets (SBJs) and transient atmospheric rivers (ARs) (e.g., Dettinger 2004; Galewsky and Sobel 2005; Ralph et al. 2006; Kim and Kang 2007; Reeves et al. 2008; Guan et al. 2010; Lundquist et al. 2010; Smith et al. 2010; Neiman et al. 2008b, 2010, 2013a; Dettinger et al. 2011; Kim et al. 2012; Ralph et al. 2013b). Landfalling extratropical cyclones along the U.S. West Coast are often accompanied by ARs, which are long (>2000 km), narrow (<1000 km) plumes of enhanced horizontal water vapor flux embedded within the broader region of generally poleward heat transport in the cyclone warm sector (Zhu and Newell 1998; Ralph et al. 2004, 2006, 2011; Neiman et al. 2008a,b, 2013b; Smith et al. 2010; Sodemann and Stohl 2013). SBJs, which were first documented during the Sierra Cooperative Pilot Project (SCPP; Reynolds and Dennis 1986) and have since been studied extensively (e.g., Parish 1982; Marwitz 1983, 1987; Smutz 1986; Neiman et al. 2010; Hughes et al. 2012; Kingsmill et al. 2013; Neiman et al. 2013a), form in response to the deceleration of stably stratified flow as it approaches the western Sierra foothills. This deceleration leads to a weakened Coriolis force, causing the flow to turn leftward toward the north end of the CV in response to the (no longer balanced) pressure gradient force. The resulting blocked flow, which is maintained in conjunction with a statically stable pressure ridge dammed against the Sierra's windward slope, parallels the range's long axis on its west side below crest level [e.g., see conceptual Fig. 13 in Neiman et al. (2013a)].

An observationally based composite study by Neiman et al. (2013a) revealed that 1) strong, moisture-laden, low-level southwesterly flow in ARs can enter a prominent gap in the coastal mountains east of San Francisco and get diverted northward by the Sierra into the SBJ within the CV and 2) the upper portion of the AR flow can override the SBJ. The composite study expanded on the observational case study of 14–16 February 2011 by Kingsmill et al. (2013), which was the first to document key interactions between SBJs and ARs. However, unlike the earlier Kingsmill contribution, it also quantified temporal and orographic linkages between SBJs, ARs, and the precipitation they generated across the northern CV and Sierra foothills. Neiman et al. (2013a) utilized a wind profiler at Sloughhouse, California (SHS; Fig. 1, Table 1), as the primary observational anchor to identify the strongest SBJ events over the northern CV during a multiyear period to investigate mean kinematic and thermodynamic characteristics of the composite SBJ and simultaneously occurring AR and to ascertain the composite orographic precipitation responses related to the SBJ and AR.

Here, we present a case study highlighting the orographic impacts of 1) an intense AR that made landfall across northern California on 23–25 October 2010 and 2) a strong SBJ observed concurrently with the landfalling AR over the northern CV. In normal years October is the beginning of the wet season in northern California, and rarely do extreme precipitation events occur at that time. However, this early season storm generated excessive

TABLE 1. Site information for the study's key observing platforms in California. Surface meteorological sites (sfc met) include a precipitation gauge. Those surface sites with soil moisture probes are noted. The precipitation gauges that comprise the northern Sierra eight-station precipitation index are labeled as "NS8SI" in the "observing platforms" column. These eight sites are also numbered 1–8 for cross referencing with Fig. 1.

Site	Three-letter name	Observing platforms	Lat (°N)	Lon (°W)	Altitude (m MSL)
Chico (NOAA)	CCO	Wind profiler, GPS, sfc met	39.69	121.91	41
Sloughhouse (NOAA)	SHS	Wind profiler, GPS, sfc met	38.50	121.21	50
Shasta Dam (NOAA)	STD	Sfc met	40.72	122.43	183
Four Trees (CA Dept. of Water Resources)	FOR	Precip. gauge	39.81	121.32	1570
Blue Canyon (NOAA)	BLU	Sfc met, soil moisture	39.28	120.71	1610
Cazadero (NOAA)	CZD	Sfc met, soil moisture	38.61	123.21	475
North Fork American River (USGS)	NFA	Streamflow	38.94	121.02	218
Austin Creek (USGS)	AUS	Streamflow	38.51	123.07	12
Pacific House (1)	PCF	Precip. gauge NS8SI	38.77	120.50	1036
Blue Canyon (2)	BYM	Precip. gauge NS8SI	39.28	120.70	1609
Sierraville (3)	SRR	Precip. gauge NS8SI	39.58	120.37	1516
Brush Creek (4)	BCM	Precip. gauge NS8SI	39.69	121.34	1085
Quincy (5)	QRD	Precip. gauge NS8SI	39.94	120.95	1042
Mineral (6)	MNR	Precip. gauge NS8SI	40.35	121.60	1486
Shasta Dam (7)	SHA	Precip. gauge NS8SI	40.72	122.42	325
Mount Shasta City (8)	MSC	Precip. gauge NS8SI	41.32	122.32	1094

precipitation across the region. Using the extreme precipitation event categories developed by Ralph and Dettinger (2012), the October 2010 storm qualifies as an "R-Cat 2" event (i.e., 300–399 mm within a 72-h period), which occurs less than 10 times per year on average across the contiguous United States. The rarity of this event (especially given its occurrence early in the season), the availability of unique remote sensing observations onshore [including those gathered by the wind profiler at Chico (CCO; Fig. 1, Table 1)], and the dearth of thorough diagnostic studies of the landfall of an extreme AR over the hydrologically crucial northern CV motivate our study.

This paper complements and expands on two recent studies (Cordeira et al. 2013; Neiman et al. 2013a) that provide a solid foundation and quantitative context within which to document the extreme nature of the 2010 storm and its impacts in the northern CV. Cordeira et al. (2013) provided a detailed diagnosis of conditions over the North Pacific prior to landfall, but they did not diagnose the mesoscale/orographic processes that led to the extreme rainfall totals over land. Neiman et al. (2013a) analyzed wind profiler observations of 13 strong storms observed simultaneously at SHS and CCO, against which this extreme event can be compared [e.g., the vertically integrated water vapor (IWV) in this event was ≥46% larger than any of those storms in the composite].[1]

Unlike the earlier composite study of Neiman et al. (2013a), the present study quantifies the orographic impacts of a landfalling AR with unusually large water vapor content and very strong horizontal water vapor transport. It also quantifies the hydrological impacts of this early season event and discusses hydrological implications of this type of extreme AR event had it occurred during the climatologically wet winter season. In short, this study is designed to answer several questions, including 1) How does the SBJ–AR of 23–25 October 2010 differ from, and expand our understanding of, previously studied events? and 2) What does this extreme event teach us about the potential impacts of similar events hereafter?

2. Instrumentation and datasets

The cornerstone observing system for this study is the 915-MHz radar wind profiler (Carter et al. 1995) located in California's CV at CCO (41 m MSL). The all-weather profiler provided hourly averaged vertical profiles of horizontal wind velocity from ~0.1 to 4.0 km above ground with ~100-m vertical resolution and ~1 m s^{-1} accuracy. It was deployed and maintained by NOAA's Earth System Research Laboratory (ESRL) in support of NOAA's HMT program and the California Energy Commission's CalWater project. The profiler winds were objectively edited using the vertical temporal continuity method of Weber et al. (1993). The height of the radar bright band, generated by melting precipitation (e.g., Battan 1973), was obtained hourly using the objective

[1] The SBJ of October 2010 (i.e., the present study) was observed by the CCO wind profiler, but it was not included in the Neiman et al. (2013a) composite catalog because the SHS wind profiler was not operating during that period.

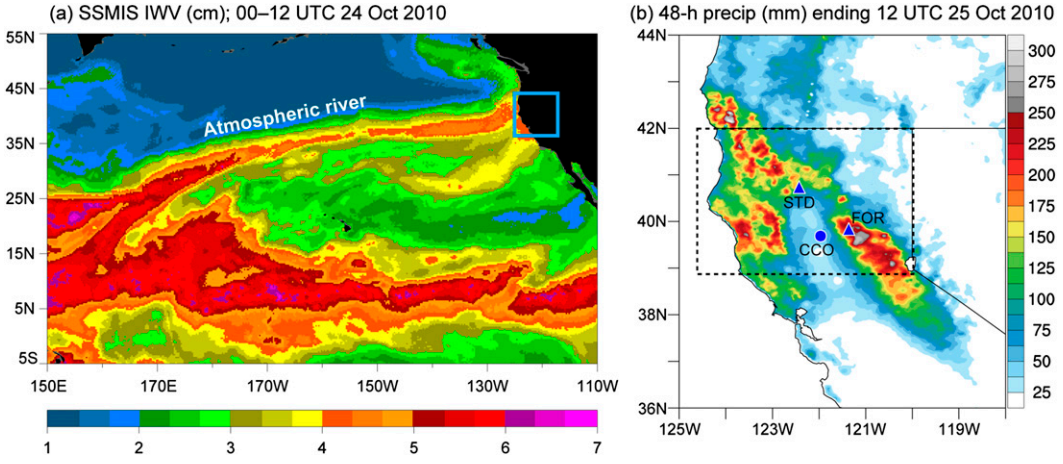

FIG. 2. Contextual observations for the case study of 23–25 Oct 2010. (a) Composite SSM/I satellite image of IWV (cm; see color bar) between ~0000 and 1200 UTC 24 Oct 2010. The blue rectangle outlines the domain of the companion accumulated precipitation analysis in the following panel and the terrain base map in Fig. 1. (b) The 48-h precipitation accumulation (mm; see color scale) from NOAA–NCEP's Stage IV gridded precipitation dataset ending at 1200 UTC 25 Oct 2010. The inner dashed rectangle shows the domain for a ranked, 48-h, areal-averaged, precipitation analysis based on the unified precipitation dataset between 1970 and 2010. The wind profiler site at CCO and the surface meteorological sites at STD and FOR are as in Fig. 1.

bright-band detection method of White et al. (2002); the bright band typically resides ~200 m below the 0°C freezing level (Stewart et al. 1984; White et al. 2002). A collocated dual-channel GPS receiver gathered 30-min tropospheric measurements of IWV with ~1 mm accuracy (Duan et al. 1996; Mattioli et al. 2007). The wind profiler site also featured a 10-m tower that measured standard surface meteorological parameters (i.e., temperature, relative humidity, surface pressure, wind velocity, and precipitation) every 2 min. Measured precipitation was analyzed from CCO and from two additional sites: Four Trees (FOR; 1570 m MSL) in the western Sierra foothills and Shasta Dam (STD; 183 m MSL) at the north end of the CV at the base of the Mt. Shasta–Trinity Alps region. See Figs. 1 and 2b and Table 1 for site locations.

Two additional sites were utilized with the same complement of tower instruments, but in the context of a soil moisture analysis: Blue Canyon (BLU; 1609 m MSL) in the western foothills of the Sierra Nevada and Cazadero (CZD; 475 m MSL) in the coastal mountains northwest of San Francisco (Fig. 1, Table 1). Both sites had probes that recorded soil moisture at 10 and 15 cm below the surface (Zamora et al. 2011). Streamflow observations from two nearby U.S. Geological Survey (USGS) gauges gathered data in the Sierra foothills on the North Fork of the American River at Lake Clementine (NFA; 218 m MSL) and in the coastal mountains on Austin Creek (AUS; 12 m MSL) (Fig. 1, Table 1). The full network of USGS stream gauges with satisfactory data quality was utilized for a regionwide analysis.

Finally, the operational network of scanning National Weather Service (NWS) Weather Surveillance Radar-1988 Doppler (WSR-88D) radars (Crum et al. 1993) provided snapshots of precipitation reflectivity during the event. Composite reflectivity images over northern California were generated by combining the data from eight radars during common 5-min intervals (Zhang et al. 2011). An exponential distance weighting function was used when multiple radar observations covered a single grid cell.

Plan-view precipitation analyses were generated from the NOAA–National Centers for Environmental Prediction (NCEP) Stage IV multisensor precipitation dataset, which is available in real time every hour and 6 h on a 4-km grid across the continental United States (Fulton et al. 1998; Lin and Mitchell 2005). In the Intermountain West, the analyses are created by distributing the precipitation gauge data onto the grid using the mountain mapper algorithm (e.g., Schaake et al. 2004) and the climatology-based Parameter-Elevation Regressions on Independent Slopes Model (PRISM; Daly et al. 1994). The grids are subjected to manual quality control at NOAA's River Forecast Centers. We also utilized the NOAA/Climate Prediction Center's (CPC) 0.25° × 0.25° horizontal resolution unified precipitation dataset (UPD), whose gridded domain is bounded by 20°–50°N latitude and 130°–55°W longitude (Higgins et al. 2007). The resolution of the UPD is coarse compared to the complex orography of northern California. However, because we average this gridded dataset across the entire region for

a climatological analysis of the synoptic precipitation, a finer horizontal resolution is not required. Finally, we used the northern Sierra eight-station precipitation index (Fig. 1, Table 1), maintained by California's Department of Water Resources. The index, which is used by water managers to gauge water supply for California, is an average of daily precipitation measured at eight sites on the flank of the northern CV in the Sierra Nevada and the adjacent Mt. Shasta–Trinity Alps region since 1922.

Synoptic and mesoscale analyses were generated from two primary data sources. First, operational ground-based reporting stations, ocean-based buoys, and ships provided hourly observations (~3-h resolution for ships) of one or more of the following variables: wind velocity, temperature, dewpoint temperature, sea level pressure, cloud cover, and precipitation. Second, the North American Regional Reanalysis (NARR) gridded dataset (Mesinger et al. 2006) provided a spatiotemporally continuous representation of the troposphere. The NARR domain covers all of North America and adjacent oceans on a 32-km horizontal grid with 45 vertical levels. The data are available at 3-h intervals from 1979 to the present. Because our primary motivation for creating NARR analyses was to assess the synoptic–mesoscale conditions offshore and over the complex orography, the 32-km grid resolution should suffice.

3. Synoptic and mesoscale context

Figure 2a provides a trans-Pacific perspective of IWV retrieved from the polar-orbiting Special Sensor Microwave Imager (SSM/I) observing platform (Hollinger et al. 1990; Wentz 1995) between 0000 and 1200 UTC 24 October 2010. A prominent, quasi-linear AR plume of enhanced IWV >~3 cm extends poleward, then eastward, from the tropical western Pacific water vapor reservoir to the Oregon–California border. Based on this imagery, and on an NARR analysis of vertically integrated horizontal water vapor transport (IVT) between 1000 and 300 hPa (Neiman et al. 2008b; shown later in this section), the AR in this case is oriented more zonally than in the SHS composite study of Neiman et al. (2013a)—from 250° to 70° rather than from 220° to 40°—and is positioned orthogonal to the long axis of northern California's Sierra Nevada and coastal ranges. Hence, assuming that the low-level flow in the AR offshore approximately parallels the IWV plume, as has been shown observationally in other AR cases (e.g., Ralph et al. 2006, 2011) and inferred from satellite feature–tracked winds and the NARR for this case (not shown), this flow matches the upslope component (i.e., the vapor transport vector projects directly onto the upslope terrain gradient vector)—an ideal scenario for orographic precipitation enhancement. It should be noted that the IVT analyses corresponding to the 20 cases composited in the SHS study (not shown) reveal that the landfalling ARs in 19 of those cases originated from a more southerly direction than in this case study. Since those cases intersected the Sierra at an oblique angle, the orographic forcing there was suboptimal.

The precipitation distribution across northern California is depicted in an analysis of 48-h accumulations from the Stage IV gridded dataset ending at 1200 UTC 25 October 2010 (Fig. 2b). The heaviest accumulations (>~200 mm) are in the northern Sierra, including near the FOR gauge, where 322 mm fell during this 48-h period. Heavy 2-day precipitation also fell in the Mt. Shasta–Trinity Alps region near the north end of the CV, where the STD gauge recorded 141 mm, as well as in the coastal ranges of northern California and southern Oregon. The flat terrain of the northern CV received far less rainfall during this 48-h period, including only 38 mm at the CCO wind profiler. Overall, the precipitation distribution across northern California bears a striking resemblance to the precipitation composite during the 20 strongest SBJ cases at SHS (Neiman et al. 2013a), all but one of which was also accompanied by an AR. A climatological analysis of areal-averaged 48-h precipitation accumulation ending at 1200 UTC 25 October 2010 [as in Cordeira et al. (2013); Fig. 2b inset box] quantifies the fact that anomalously heavy precipitation fell during this storm: it was the fourteenth wettest 2-day event overall between 1970 and 2010 and the largest 2-day event for the month of October for that same 40-yr period.[2]

A time series of cumulative daily rainfall from the northern Sierra eight-station precipitation index for water year 2011 (i.e., from 1 October 2010 to 30 September 2011; Fig. 3) reveals that the storm studied here produced the first significant precipitation event of that water year, totaling ~180 mm during the 3-day period on 23–25 October. Significantly, the 3-day total represents 237% of an average October (i.e., 76 mm) and 14% of an average water year (i.e., 1270 mm), and it contributed ~10% to the very wet water year of 2011 (i.e., 1847 mm), which itself was 145% of normal. For reference, a companion cumulative precipitation trace for the 76-yr average between 1922 and 1998 is plotted on the same graph. By all accounts, including from the ranked gridded

[2] The areal averages were computed from the NOAA/CPC's UPD at 1200 UTC of each day by dividing the sum of all daily precipitation values on the 0.25° grid by the number of grid cells. They were then ranked.

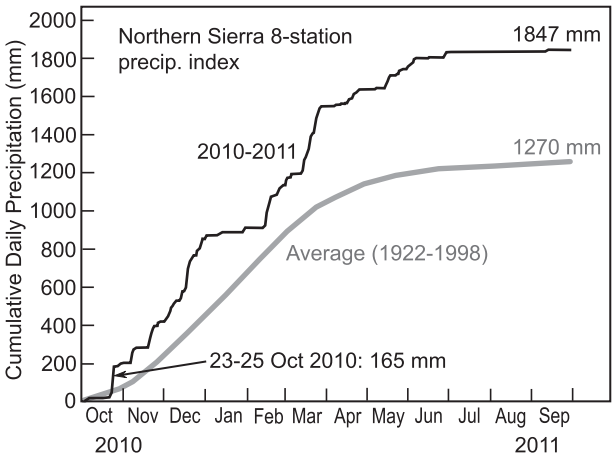

FIG. 3. Cumulative daily precipitation time series (mm) from the northern Sierra eight-station index for water year 2011 (i.e., from 1 Oct 2010 to 30 Sep 2011; thin black line) and for the 76-yr average from 1922 to 1998 (thick gray line). The end-of-water-year precipitation totals are also shown numerically for both time series, as is the precipitation total for the period 23–25 Oct 2010.

precipitation analysis described earlier, this event was anomalous, especially for the month of October. However, because less than 50 mm of precipitation fell during the dry season in the previous four months, the streamflow response in this early season event was muted relative to what often occurs later in the cool season when soils are preconditioned (i.e., already moistened) for quick runoff response (e.g., Ralph et al. 2013b), as will be quantified in section 5.

Using NOAA–NCEP's Climate Forecast System Reanalysis gridded dataset with 0.5° × 0.5° horizontal resolution (Saha et al. 2010), Cordeira et al. (2013) carried out a detailed synoptic-scale analysis of this AR event over the North Pacific. They demonstrated that water vapor was transported from western North Pacific tropical cyclones into the equatorward entrance region of an intensifying North Pacific jet stream and developing pair of zonally elongated ARs in environments characterized by large convective available potential energy. These ARs were maintained and subsequently merged over the central and eastern North Pacific on the anticyclonic shear side of a strong and zonally extended North Pacific jet stream in an environment characterized by frontogenesis and quasigeostrophic (QG) ascent. A water vapor budget analysis revealed that decreases in IWV via rainout along the AR were offset largely by IWV flux convergence in the presence of frontogenesis and, to a lesser extent, evaporation (i.e., upward sea surface latent heat fluxes) from the ocean surface.

The case study presented here provides a complementary and expanded analysis to that of Cordeira et al. (2013), focusing on the landfall of the intense AR across northern California. This includes diagnosis of the evolution of an SBJ, the overrunning of the SBJ by the AR, and the role of these features in controlling orographic precipitation in northern California. Figure 4 displays NARR synoptic analyses at 0600 UTC 24 October 2010, roughly corresponding to the time of the SSM/I IWV satellite imagery in Fig. 2a. An IVT analysis (Fig. 4a) portrays a narrow, quasi-zonally oriented AR offshore with strong vapor fluxes that coincide with the SSM/I IWV plume (Fig. 2a). The enhanced plume of IVT arcs cyclonically around a storm centered west of Vancouver Island (Fig. 4b), and the southern periphery of this arc is impacting northern California with IVT oriented roughly orthogonal to the long axis of the Sierra (i.e., from ~250°). The core of the AR aligns approximately with the leading edge of a polar cold front offshore on the anticyclonic shear side of a strong jet stream aloft (Fig. 4b) that Cordeira et al. (2013) referred to as the zonally extended North Pacific jet. Although weak warm-air advection and implied isentropic ascent covers northern California within the cyclone warm sector, the northern CV resides beneath the right exit region of the straight jet aloft, which is a favored region of dynamical subsidence (e.g., Beebe and Bates 1955). Nevertheless, significant rain is already falling by this time in northern California's mountains (shown later in Fig. 8c). The ascending left exit branch of the jet's circulation is farther north over northern Oregon and Washington.

Midtropospheric cyclonic vorticity advection (CVA) at 500 hPa (Fig. 4c) and its implied QG forcing for ascent (given the assumption CVA increases with height) also resides north of California at 0600 UTC 24 October. A companion analysis of 700-hPa **Q**-vector diagnostics (e.g., Morgan 1999; Fig. 4d) places strong **Q**-vector convergence and its midtropospheric QG forcing for ascent near the Washington–Oregon coast, while weak **Q**-vector divergence and its related forcing for subsidence covers much of California. The area of implied upward-motion forcing associated with the cold-frontal baroclinic zone, the region of CVA, and the exit region of the jet stream subsequently migrates southward over the northern CV later in the day (not shown). However, between 0600 UTC 24 October and later on 24 October, NARR **Q** vector and related analyses (not shown) do not support strong synoptic ascent across northern California in the warm sector during the initial AR landfall. Nevertheless, those analyses show strengthening IVT across northern California, as well as moist neutral static stability below 700 hPa within the AR offshore (in accord with previous AR studies: Ralph et al. 2005b, 2011; Neiman et al. 2008a, 2013b). The result is that heavy rain fell in the mountains flanking the northern CV during AR landfall (described in more detail in section 4).

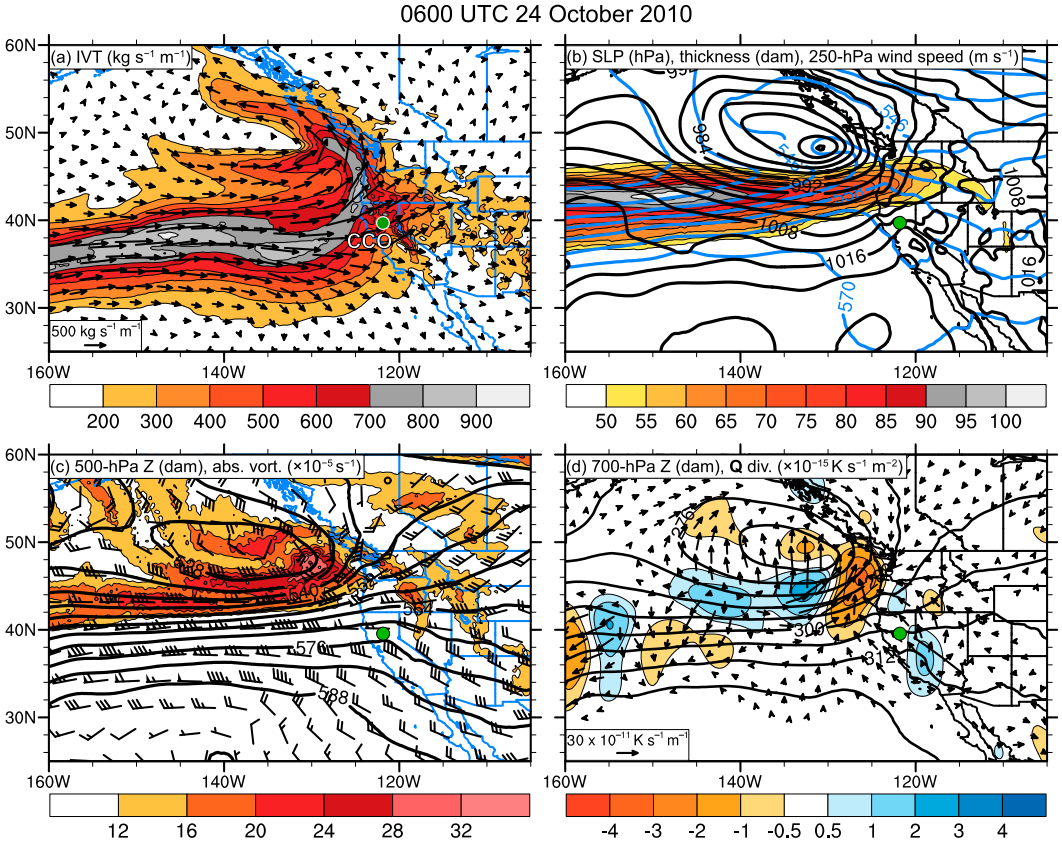

FIG. 4. Synoptic plan view analyses at 0600 UTC 24 Oct 2010 from the NARR gridded dataset: (a) 1000–300-hPa IVT [$\mathrm{kg\,s^{-1}\,m^{-1}}$; color fill with vectors (inset magnitude scale shown)]; (b) SLP (hPa; black contours), 1000–500-hPa thickness (dam; blue contours) and 250-hPa wind speed ($\mathrm{m\,s^{-1}}$; color fill); (c) 500-hPa geopotential height (Z; dam; black contours), absolute vorticity ($\times 10^{-5}\,\mathrm{s^{-1}}$; color fill), and wind velocities (flags = $25\,\mathrm{m\,s^{-1}}$; barbs = $5\,\mathrm{m\,s^{-1}}$; half barbs = $2.5\,\mathrm{m\,s^{-1}}$); and (d) 700-hPa geopotential height (Z; dam; black contours), **Q** vectors ($\times 10^{-11}\,\mathrm{K\,m^{-1}\,s^{-1}}$; inset magnitude scale shown), and **Q**-vector divergence ($\times 10^{-15}\,\mathrm{K\,m^{-2}\,s^{-1}}$; color fill). The wind profiler site at CCO is marked with a circle.

Early studies (e.g., Lowndes 1968; Browning et al. 1974) have shown that orographic precipitation can be heavy within potentially unstable/neutral warm sectors of extratropical cyclones that do not contain significant large-scale lift, because the potential instability/neutrality is preserved until acted upon by orographic lift.

Figure 5 portrays the surface conditions over northern California during the AR landfall and SBJ evolution. At 1800 UTC 23 October 2010 (Fig. 5a), weak poleward-directed flow is observed in the northern CV beneath a mesoscale sea level pressure (SLP) ridge created by terrain blocking from the Sierra. During this time, scattered light rain is falling in the northern Sierra (see also the radar image in Fig. 6a). The accumulated 12-h rainfall ending at this time is light across northern California (Fig. 7a). For the 12-h period ending at 0600 UTC 24 October (Fig. 5b), the terrain-induced SLP ridge is maintained over the northern CV, while strengthening downgradient south-southeasterly flow in the northern CV represents a surface reflection of the intensifying SBJ during the approach of the AR from the northwest. A surface manifestation of the AR is discerned over northwestern California and southern Oregon in the form of a strong, southeastward-directed, pre-cold-frontal SLP gradient. Rainfall at this time encompasses much of northern California, with heavier rains across orographically favored locales in the northern Sierra, the northern terminus of the CV, and the coastal ranges. Companion radar imagery (Fig. 6b) confirms this, as well as documenting a solid band of rainfall with the AR straddling the California–Oregon border. The 12-h rainfall (Fig. 7b) shows heavier accumulations (~50 mm) in the orographically favored regions. By 1800 UTC 24 October (Fig. 5c), the entire CV contains coherent, poleward-directed, downgradient SBJ flow, although this flow is strongest in the northern CV where the remnant SLP ridge persists. The strong SLP gradient linked with the AR now lies across the San Francisco

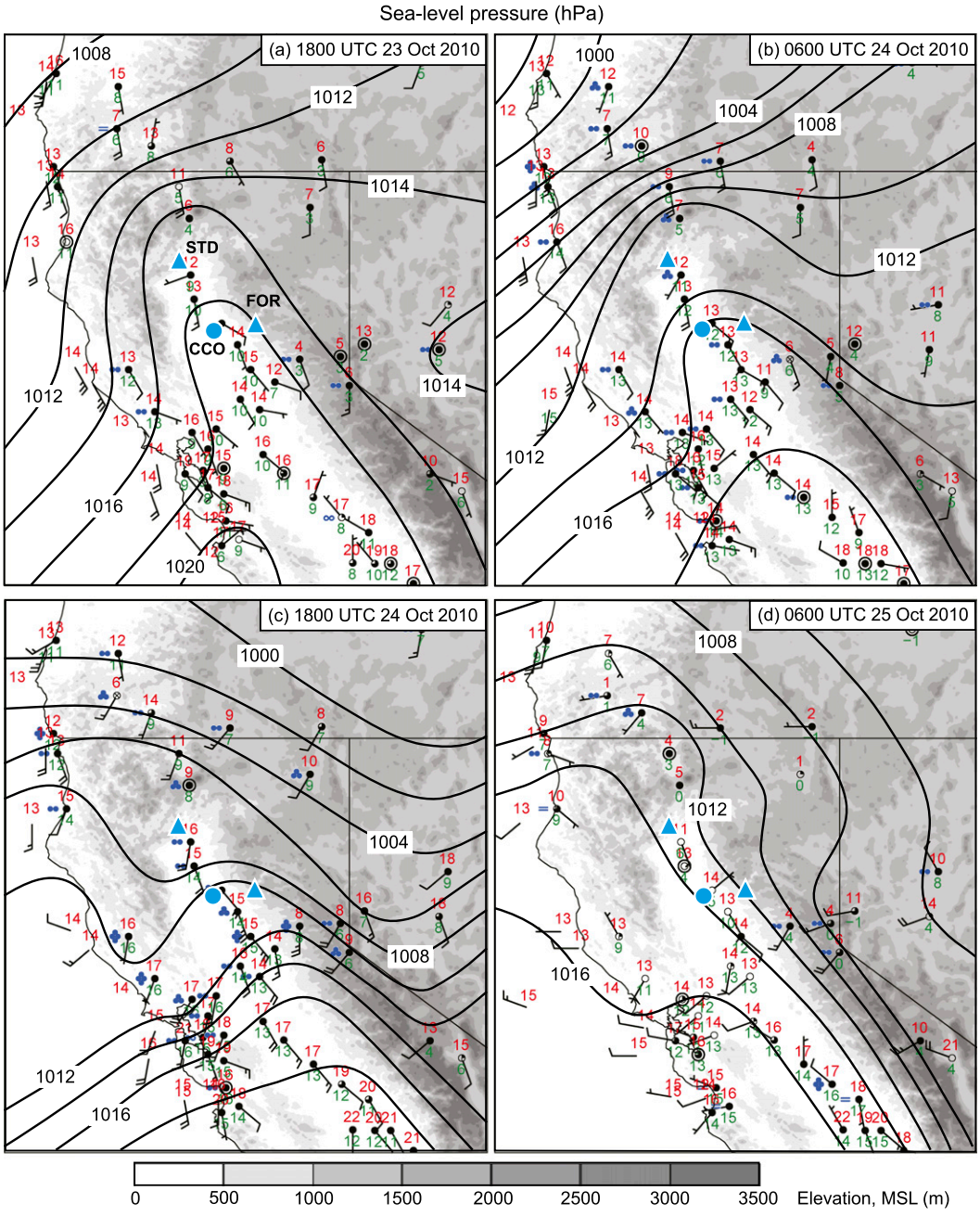

FIG. 5. Ground- and ocean-surface observations and manual analyses of SLP (hPa) plotted on a terrain base map (m MSL; see grayscale) at (a) 1800 UTC 23 Oct, (b) 0600 UTC 24 Oct, (c) 1800 UTC 24 Oct, and (d) 0600 UTC 25 Oct 2010. Wind barbs are as in Fig. 4c. Temperature and dewpoint values (°C; red and green, respectively) are shown with each reporting station, as is rain intensity when applicable (two, three, and four blue dots denote light, moderate, and heavy rain intensity, respectively). The wind profiler site at CCO and the surface meteorological sites at STD and FOR are as in Fig. 1.

Bay (SFB) gap, where a warm and moist southwesterly airstream (with temperatures and dewpoints of 16°–17°C) enters the CV and subsequently turns northward into the SBJ flow, mirroring the composite AR–SBJ results of Neiman et al. (2013a). At this time, widespread moderate to heavy rains cover northern California in response to the combined impacts of orographic lift and transient synoptic and frontal-scale ascent (see also Fig. 6c). Rainfall totals across northern California are largest during this 12-h period (Fig. 7c). At 0600 UTC 25 October

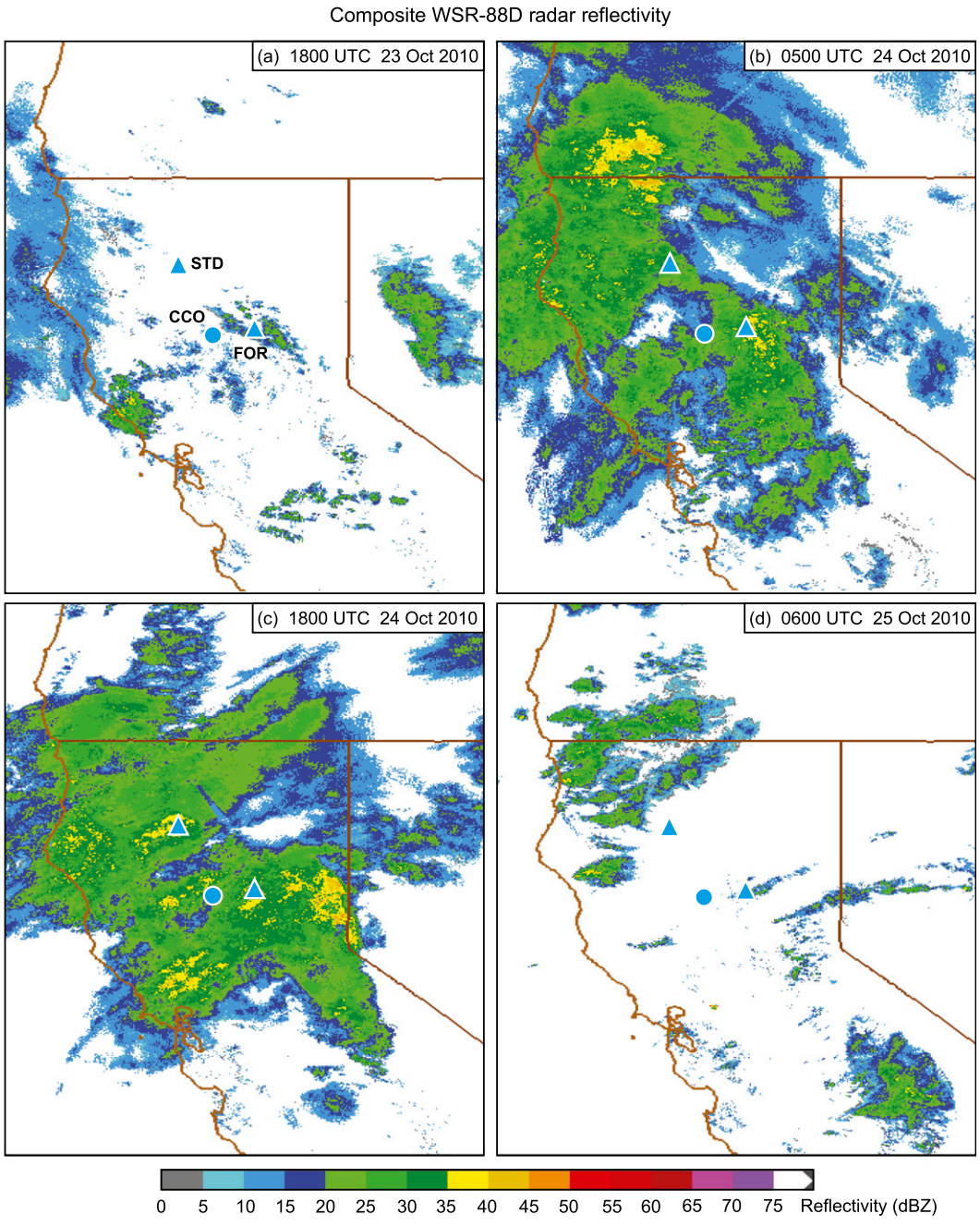

FIG. 6. Composite images of radar reflectivity (dBZ) from the operational WSR-88D radar network at (a) 1800 UTC 23 Oct, (b) 0500 UTC 24 Oct, (c) 1800 UTC 24 Oct, and (d) 0600 UTC 25 Oct 2010. The radar image at 0600 UTC 24 Oct 2010 was not shown because of poor data quality at that time. The wind profiler site at CCO and the surface meteorological sites at STD and FOR are as in Fig. 1.

(Fig. 5d), cooler and drier post-cold-frontal conditions cover northern California, with building high pressure and weak flow. Scattered light rain persists over northern California (see also Fig. 6d), while the region of maximum 12-h rainfall has shifted southward along the Sierra Nevada (Fig. 7d) with the passage of the AR and trailing cold front.

4. Wind profiler perspective

a. Observed vertical temporal structure

Observations at and near CCO provide a unique local perspective on the AR landfall and SBJ evolution in the northern CV between 0000 UTC 23 October and 0800 UTC 25 October 2010 (Fig. 8). A time–height

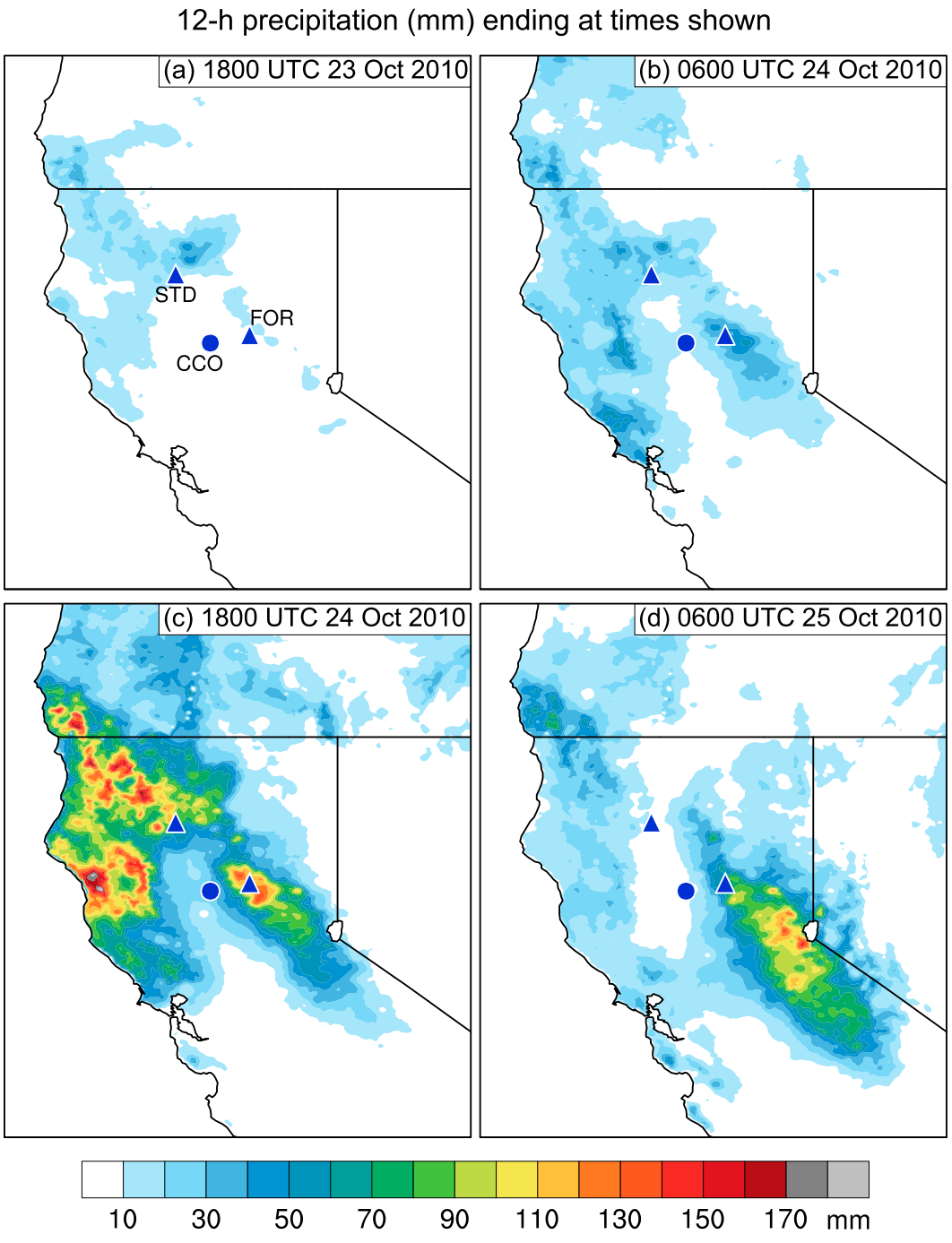

FIG. 7. The 12-h precipitation accumulation (mm; see color scale) from NOAA–NCEP's Stage IV gridded precipitation dataset ending at (a) 1800 UTC 23 Oct, (b) 0600 UTC 24 Oct, (c) 1800 UTC 24 Oct, and (d) 0600 UTC 25 Oct 2010. The wind profiler site at CCO and the surface meteorological sites at STD and FOR are as in Fig. 1.

analysis of hourly wind profiles and AR-parallel (i.e., Sierra perpendicular) isotachs at CCO (Fig. 8a) shows the temporal descent of enhanced shear associated with a warm front from 4 km MSL at 0800 UTC 23 October to ~1 km MSL (i.e., atop the SBJ in Fig. 8b) between 0700 and 1900 UTC 24 October. An axis of geostrophic warm-air advection [based on the thermal wind diagnostic in Neiman and Shapiro (1989)] coincides with the descent of the warm frontal shear layer, while additional warm-advection filaments descend from the

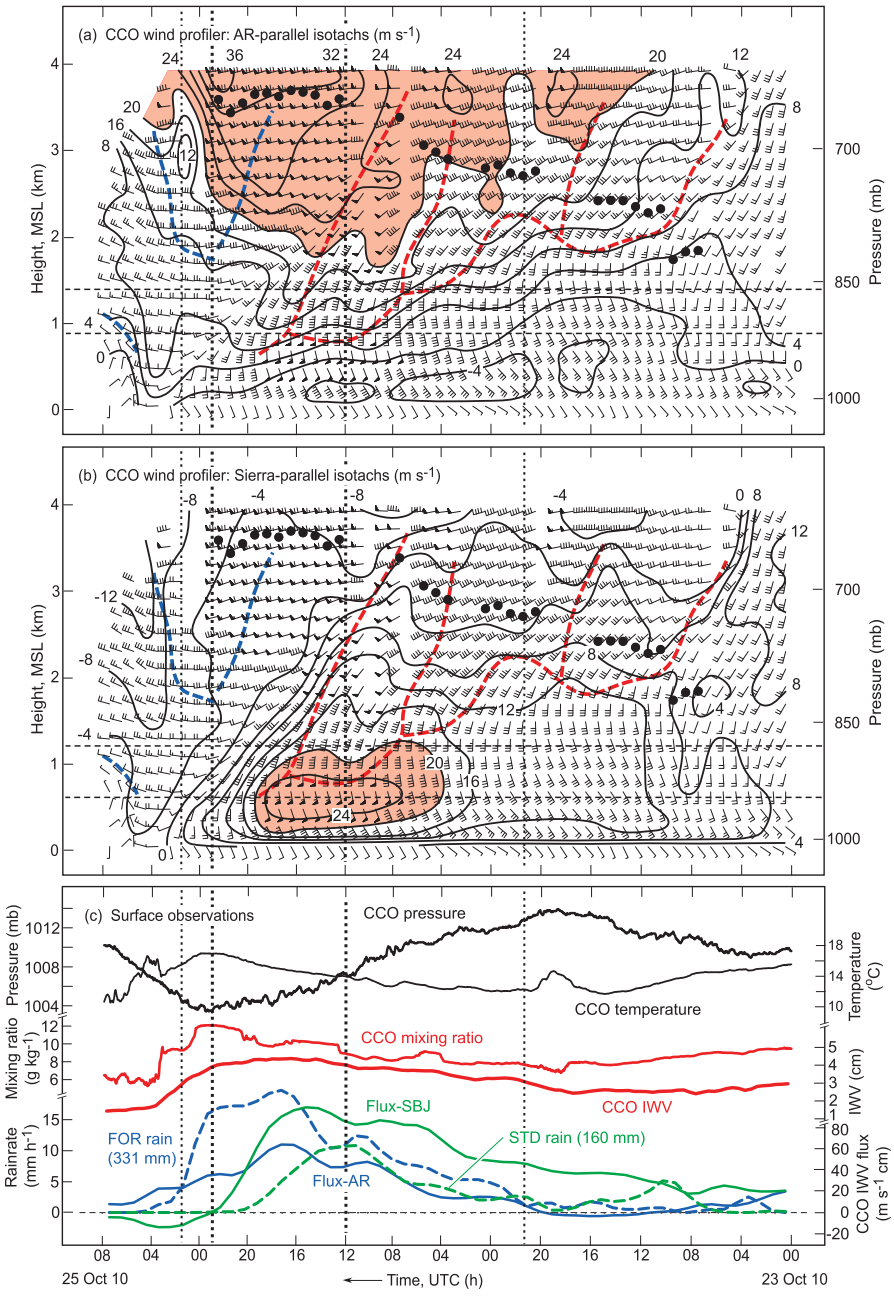

FIG. 8. Time series of observations from CCO and nearby precipitation gauges between 0000 UTC 23 Oct and 0800 UTC 25 Oct 2010, with time increasing from right to left to portray the advection of transient synoptic features from west to east. The thin (thick) vertical dotted lines mark the outer temporal bounds of IWV > 3 (> 4) cm. (a) Time–height section of hourly averaged wind profiles (flags and barbs are as in Fig. 4c), AR-parallel isotachs (black contours; m s^{-1}; directed from 250°; red shading >20 m s^{-1}), bright-band melting-level heights (bold black dots), and axes of maximum thermal wind-derived (i.e., geostrophic) warm and cold advection (red and blue dashed lines, respectively). Every wind profile and every other range gate is plotted. (b) As in (a), but for Sierra-parallel isotachs (m s^{-1}; directed from 160°). The horizontal thin dashed lines in (a) and (b) show the vertical bounds for the AR and SBJ orographic controlling layers, respectively. (c) Time series of surface pressure (hPa; thick black), surface temperature (°C; thin black), surface water vapor mixing ratio (g kg^{-1}; thin red), IWV (cm; thick red), the upslope IWV flux in the orographic controlling layer for the AR component (blue solid; Flux-AR: from 250°, 0.9–1.4 km MSL) and SBJ component (green solid; Flux-SBJ: from 160°, 0.6–1.2 km MSL) of the flow at CCO, and time series of hourly rain rate (mm h^{-1}) at FOR (blue dashed) and STD (green dashed). Storm total precipitation (mm) is given in parentheses for each site.

warm sector to this same shear layer, resulting in incremental rises in the altitude of the bright-band melting level from 1.8 to 3.8 km MSL (i.e., to an altitude well above the Sierra crest). The contiguous area of strong AR-parallel (>20 m s^{-1}), west-southwesterly flow on the warm side of the warm front (i.e., above the warm frontal shear zone) between 2130 UTC 23 October and 0130 UTC 25 October coincides with IWV > 3 cm and marks the AR airstream aloft. The moist conditions also correspond to the core period of shallow, Sierra-parallel, south-southeasterly flow within the SBJ (Fig. 8b).

The AR-parallel isotachs in Fig. 8a also capture the temporal ascent of the polar cold frontal shear zone, from atop the SBJ core at ~1800 UTC 24 October to 4 km MSL at 0000 UTC 25 October. The cold frontal passage aloft, which marks the onset of the SBJ decay below (Fig. 8b), is accompanied by a prominent wind shift from strong southwesterly to weaker westerly and geostrophic cold advection. The wind profiler does not observe a drop in the melting level with the cold frontal passage aloft, because precipitation at CCO ends before the cold front ascends to the melting level. Also, the cold front does not penetrate downward into the SBJ airstream, likely because of enhanced stable stratification in the SBJ, so its interaction with the SBJ takes on the appearance of a terrain-forced, warm frontal occlusion. Bergeron (1937) referred to such a feature as a quasi-stationary orographic occlusion. Companion IWV measurements exceed 4 cm during an 11-h period of AR conditions on either side of the initial cold frontal detection at 1800 UTC (i.e., between 1200 and 2300 UTC 24 October), and a maximum IWV value of 4.37 cm occurs at 1645 UTC (Fig. 8c) in the immediate pre-cold-frontal environment where frontally forced water vapor convergence in ARs is often strong (e.g., Cordeira et al. 2013; Neiman et al. 2013b).

Time series traces (Fig. 8c) provide additional insight into the meteorological evolution across the northern CV. The surface pressure at CCO exhibits a sinusoidal pattern, with rising pressure during the onset of SBJ conditions prior to 2000 UTC 23 October, falling pressure during the AR landfall, a pressure trough at 2300 UTC 24 October coinciding with the cold frontal passage aloft, then rising pressure thereafter. Surface temperature and mixing ratio at CCO show cooling and drying during the formation of the SBJ prior to 1500 UTC 23 October, while the IWV remains steady. As the SBJ intensifies after 2200 UTC 23 October, surface warming and moistening ensues and then becomes more dramatic after 0800–1200 UTC 24 October. Based on the SLP analysis at 1800 UTC 24 October (Fig. 5c) and the composite results in Neiman et al. (2013a), the enhanced warming and moistening likely occurs because warm, moist, low-level air associated with the AR enters the SFB gap and turns northward up the CV while becoming incorporated into the SBJ. The IWV increases to >4 cm during this period in response to the combined impacts of moistening in the shallow SBJ and the landfalling AR aloft. During the decay of the SBJ after ~1800 UTC 24 October, the surface temperature and mixing ratio continue to increase for 6 more hours despite layer-mean IWV drying with the cold frontal passage aloft, thus mirroring the composite SBJ behavior in Neiman et al. (2013a). The surface temperature and mixing ratio finally start declining at 0000 UTC 25 October, although the temperature briefly rises again at ~0300 UTC in response to drying post-cold-frontal westerly flow mixing down to the surface, replacing the potentially cooler remnant SBJ airstream. These observations support the concept of a terrain-forced warm occlusion.

b. *Orographic precipitation diagnostics*

Figure 8c contains two time series of upslope IWV flux at CCO, as well as rain-rate traces at FOR and STD. The time series labeled Flux-AR represents the hour-to-hour product of IWV and the component of the flow directed from 250° (i.e., perpendicular to the Sierra crest and parallel to the AR) in the layer between 0.9 and 1.4 km MSL (marked on Fig. 8a); it is orographically coupled with the FOR observations in the Sierra (i.e., the Sierra couplet, where FOR is 52 km downwind of CCO). In contrast, the Flux-SBJ trace uses the component of the flow from 160° (i.e., perpendicular to the Mt. Shasta–Trinity Alps terrain and parallel to the SBJ) in the layer between 0.6 and 1.2 km MSL (see Fig. 8b); it is orographically coupled with the STD observations at the north end of the CV (i.e., the Trinity couplet, where STD is 122 km downwind of CCO). The altitude of the IWV fluxes plotted for each couplet is based on the height of the local linear correlation maximum (i.e., the orographic controlling layer) between the hourly upslope IWV flux and the hourly rain rate at that couplet (see Fig. 9). The methodology and rationale for adopting this approach is provided in Neiman et al. (2002, 2009). Because the early season AR yielded very high melting levels above the Sierra crest, only rain fell in the mountains, thus providing far more accurate hourly precipitation rate measurements than if snow had fallen.

Comparison of the IWV flux and rain-rate traces at each couplet underscores the close temporal relationship and orographic link between these variables, and it emphasizes the impact of the AR (SBJ) on orographic precipitation forcing in the northern Sierra (at the north end of the CV), comparable to the composite results in Neiman et al. (2013a). The orographic forcing and resultant precipitation occurred for many hours prior to

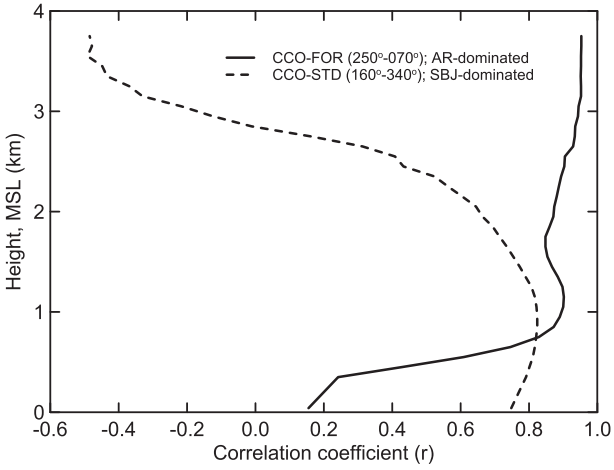

FIG. 9. Vertical profiles of linear correlation coefficient for the period 0000 UTC 23 Oct through 0800 UTC 25 Oct 2010, based on hourly averaged profiles of upslope IWV flux at Chico (CCO) vs hourly precipitation rate at FOR (solid curve) and at STD (dashed curve). The upslope direction for the Sierra and Trinity couplets (CCO–FOR and CCO–STD, respectively) are from 250° and 160°, respectively.

the onset of synoptic and frontal-scale ascent across the region (e.g., Fig. 4). These traces also highlight the fact that the orographic precipitation efficiency is greater in the Sierra than at the north end of the CV (i.e., weaker IWV fluxes yield greater rain rates in the Sierra) and may reflect the presence of weaker static stability in the AR aloft than in the shallow SBJ, as was documented in the composite study by Neiman et al. (2013a). At the Sierra (Trinity) couplet, the fluxes and rain rates intensify in tandem with the strengthening AR (SBJ). Additionally, at the Sierra couplet the strongest orographic forcing and heaviest precipitation occur at the tail end of the SBJ core when the wind direction in the controlling layer shifts from southerly to southwesterly in the moist (i.e., IWV $>$ 4 cm) AR airstream and within the cold frontal zone [i.e., when the flow becomes more perpendicular to the axis of the Sierra; as in the composite study by Neiman et al. (2013a)]. In contrast, the strongest orographic forcing and heaviest precipitation at the Trinity couplet coincides with the shallow core of SBJ flow at CCO, which is directed northward up the CV. At both couplets, the precipitation ends following the passage of the cold front aloft, which occurs several hours later at the more southern gauge at FOR because of the equatorward migration of the front. During the 56-h period shown in Fig. 8, 331 mm of rain fell at FOR, 160 mm at STD, and only 39 mm at the flat CCO site, thus further highlighting the orographically forced character of the precipitation.

Vertical profiles of linear correlation coefficient are shown in Fig. 9; they are based on the hourly averaged profiles of upslope IWV flux measured in 500-m layers at CCO versus the hourly rain rate at either FOR or STD. The correlation profiles at the Sierra and Trinity couplets (with upslope flow directions from 250° and 160°, respectively) exhibit distinctive characteristics that reflect orographic forcing by the AR and SBJ, respectively. The correlations in these profiles are maximized at the Sierra (Trinity) couplet when the flows used in the calculation are the components directed from 250° (160°) and decrease when other flow orientations are used, a result that is in keeping with a greater impact of the AR (SBJ) on the orographic precipitation forcing in the northern Sierra (at the north end of the CV). The Sierra couplet contains a local correlation coefficient maximum of 0.90 at 1.15 km MSL (providing our best estimate of the orographic controlling layer in this locale) associated with the transport of water vapor aloft within the landfalling AR, and it decreases sharply downward to the surface within the shallow SBJ. Although the general character of this segment of the correlation profile mirrors its composite counterpart in Neiman et al. (2013a), the altitude of the controlling layer is 0.35 km lower for the present case study. Above 1.15 km MSL, the correlation decreases slightly with increasing height, then increases again, quite likely because of transient synoptic-scale forcing aloft. The Trinity couplet suggests the greater importance of the SBJ in generating orographically enhanced precipitation at the north end of the CV. A shallower correlation maximum of 0.82 at 0.9 km MSL resides within the SBJ and suggests an important role for the strong poleward water vapor transport toward the Shasta–Trinity region. The persistence of high correlations downward to the surface is interpreted as being due to the shallow character of the SBJ flow. These characteristics conform to those in the composite study (Neiman et al. 2013a), although the altitude of the orographic controlling layer is 0.15 km higher for the case study. Above the SBJ-induced orographic controlling layer, the correlation decreases steadily with increasing height, in contrast to the composite study that exhibits a more modest decrease with increasing height. The composite correlation profiles differ from the case study for both the Sierra and Trinity couplets in ways that likely reflect the extreme character of this case (as described next).

c. *Quantifying the extreme nature of the October 2010 event*

To further quantify the extreme character of this event, the case study observations from CCO are summarized here in an effort to compare and contrast with key characteristics of the AR, SBJ, and associated precipitation of each of the 13 events that comprise the CCO composite

analyses in Neiman et al. (2013a). To aid in this comparison, Table 2 was produced; most of the information in this table was not presented in Neiman et al. (2013a). The following comparisons highlight which characteristics of the case study were most extreme and which were not:

- Maximum IWV in the case study is 4.37 cm, which is roughly twice the composite mean and ≥146% of the maximum IWV in any of the 13 events.
- The case study occurred almost 1 month earlier in the autumn than the earliest of the 13 events, which likely contributed to the higher value of IWV.
- The 36-h duration of SBJ conditions in the case study (between 1030 UTC 23 October and 2230 UTC 24 October 2010) is the second longest relative to the 13 events and in the top 8% of the 211 SBJ cases studied at CCO between 2000 and 2007 (Neiman et al. 2010).
- The maximum AR component of the winds aloft is 39.1 m s^{-1} in the case study, which is more than 150% of the 13-case composite mean of 24.8 m s^{-1}.
- The maximum SBJ flux (Flux-160) of 99.3 m s^{-1} cm for the case study is 225% of the composite mean and 135% of the largest event in the composite. The storm total of SBJ fluxes integrated over the duration of the 36-h case study is 1632 m s^{-1} cm, which is 220% of the composite mean and 146% of the largest event in the composite.
- The maximum AR flux (Flux-250) of 64.2 m s^{-1} cm for the case study is 355% of the composite mean and 155% of the largest event in the composite. The storm total of AR fluxes for the case study is 921 m s^{-1} cm, which is 320% of the composite mean and 168% of the largest event in the composite.
- The storm total rainfall of 118 mm (293 mm) at STD (FOR) for the case study is 227% (480%) of the composite mean and 150% (331%) of the largest event in the composite.
- The SBJ maximum wind speed for the case study is 27.6 m s^{-1}, which is only 17% greater than the composite mean.

In short, the case study was extreme in terms of its water vapor content, AR wind speeds, SBJ duration, and water vapor fluxes, while the SBJ winds were near average. The large IWV was likely influenced by the early season nature of the event, for which sea surface temperatures (SSTs) were warmer than in winter. These combined to produce highly anomalous rainfall totals.

5. Hydrological implications

The hydrological response to this extreme early season AR is quantified via a time series analysis of rainfall, soil moisture, and streamflow (Fig. 10) recorded at representative observing couplets in California's coastal mountains (CZD–AUS) and in the northern Sierra (BLU–NFA; Fig. 1, Table 1). Rainfall at CZD (Fig. 10a) began at ~1200 UTC 23 October 2010 and persisted for 30 h, totally 215 mm. The initial 24-h period of rain was moderate intensity due largely to orographic forcing, followed by a final 6-h burst reflecting the combined impacts of orographic forcing and AR landfall. Total rainfall in the Sierra at BLU (258 mm; Fig. 10d) exceeded that at CZD, although the time series at BLU reveals a uniform increase in intensity during the event, culminating in the heaviest rains between 1400 UTC 24 October and 0000 UTC 25 October with the strongest orographic forcing and AR landfall. The soil volumetric water content at both sites was quite dry (~10%) at a depth of 10 and 15 cm prior to the onset of the storm (Figs. 10b,e) because little rain fell during the preceding dry season. The ground moistened during the initial rainfall and eventually reached field capacity (Veihmeyer and Hendrickson 1931; Hillel 1998) following ~100 mm of rain at each site. The most intense rains at each site, occurring during the AR landfall, resulted in a several-hour period of enhanced soil water content that significantly exceeded field capacity. Thereafter, the ground started drying once the rains ceased. Companion hydrographs at AUS and NFA (Figs. 10c,f) show scant base flow prior to the onset of the storm because of the dry antecedent soils. At AUS, the flow increased as the soil water content approached field capacity and then spiked at ~100 m^3 s^{-1} shortly after the field capacity was exceeded during the heaviest rains. The hydrograph at NFA (Fig. 10f) does not show discharge before 2100 UTC 24 October even though the river stage began increasing after 0300 UTC 24 October. The gauge station at this location is located ~15 m upstream of the North Fork dam, which is a debris dam. The rating curve at that location is only applicable when the flow tops the dam (i.e., when the stage exceeds 0 m). Thus, flow can be increasing in the channel above the dam prior to overtopping. A peak flow of ~300 m^3 s^{-1} at NFA occurred after the volumetric soil water content significantly exceeded field capacity. The median (very low) streamflow values for the period of record at AUS and NFA highlight the noteworthy hydrological nature of this early season event.

Expanding on the time series analyses above, a regional streamflow perspective across northern California is shown in Fig. 11. This analysis is based on the ranking of daily averaged flows during four consecutive days (i.e., 23–26 October 2010; add 7 h to convert from local time to UTC) relative to all available October days observed historically between 1950 and 2012. The ranked analyses require at least 20 Octobers of daily records at each site. On 23 October 2010 (Fig. 11a), streams

TABLE 2. Chronological list of the 13 SBJ cases observed at SHS that were used as the baseline for the multicase composite analysis presented in Neiman et al. (2013a). The meteorological attributes for these cases are obtained from the hourly observations at CCO for the ±12-h period surrounding the time of the SBJ core observed at SHS. The variable V_{max} is the maximum (i.e., core) value of the SBJ component of the flow (from 160°). The columns with "Flux-160" refer to IWV flux in the direction of the SBJ component of the flow (from 160°) in the orographic controlling layer between 0.5 and 1.0 km MSL, and the columns with "Flux-250" refer to IWV flux directed orthogonal to the northern Sierra (from 250°) in the orographic controlling layer between 1.3 and 1.8 km MSL. The 13-case composite-mean values are also shown, as are the values for this case study, where SBJ conditions persisted for 36 h—from 1030 UTC 23 Oct to 2230 UTC 24 Oct 2010. For the case study, the Flux-160 and Flux-250 values are valid at the controlling layers of 0.6–1.2 km MSL and 0.9–1.4 km MSL, respectively. The integrated-flux values include only positive hourly flux measurements summed over the duration of each event.

Case	SBJ core time and date at SHS	SBJ Duration (h)	SBJ V_{max} magnitude ($m\,s^{-1}$)	SBJ V_{max} altitude (m MSL)	IWV max (cm)	Flux-160 max ($m\,s^{-1}$ cm)	Flux-250 max ($m\,s^{-1}$ cm)	Flux-160 integrated ($m\,s^{-1}$ cm)	Flux-250 integrated ($m\,s^{-1}$ cm)	Precip. STD (mm)	Precip. FOR (mm)
1	1630 UTC 19 Jan 2010	40	40.1	1585	2.10	63.3	21.8	1117	233	52.8	63.0
2	0530 UTC 5 Feb 2010	19	33.2	1181	2.44	65.9	18.4	960	139	79.0	50.8
3	0530 UTC 24 Feb 2010	23	27.0	1181	2.31	52.1	20.6	759	161	40.1	66.0
4	0230 UTC 21 Nov 2010	9	22.0	1181	1.95	36.4	17.3	528	242	61.0	48.8
5	1030 UTC 6 Dec 2010	10	24.9	777	2.72	55.8	30.8	856	352	57.4	78.2
6	0830 UTC 22 Dec 2010	17	21.5	1282	2.49	37.1	13.4	633	148	38.9	27.4
7	0530 UTC 29 Dec 2010	12	27.2	676	3.00	73.4	41.4	869	547	65.0	88.4
8	1830 UTC 14 Feb 2011	20	31.6	979	2.25	57.6	27.3	966	384	62.2	39.6
9	0830 UTC 16 Feb 2011	8	25.5	777	2.32	55.5	37.9	697	529	31.2	66.0
10	1430 UTC 25 Feb 2011	15	12.3	777	1.79	19.5	14.8	222	231	4.8	63.0
11	1330 UTC 2 Mar 2011	17	29.9	1282	2.28	51.5	23.9	850	322	62.7	52.8
12	1730 UTC 18 Mar 2011	9	21.7	1484	1.97	37.8	20.2	649	362	54.1	79.2
13	0730 UTC 20 Mar 2011	34	38.4	1484	2.01	58.8	13.8	998	170	68.1	70.1
	13-case composite mean	17.9	23.5	1232	2.13	44.2	18.1	742	288	52.1	61.0
	Case study Oct 2010	36	27.6	577	4.37	99.3	64.2	1632	921	118.5	292.6

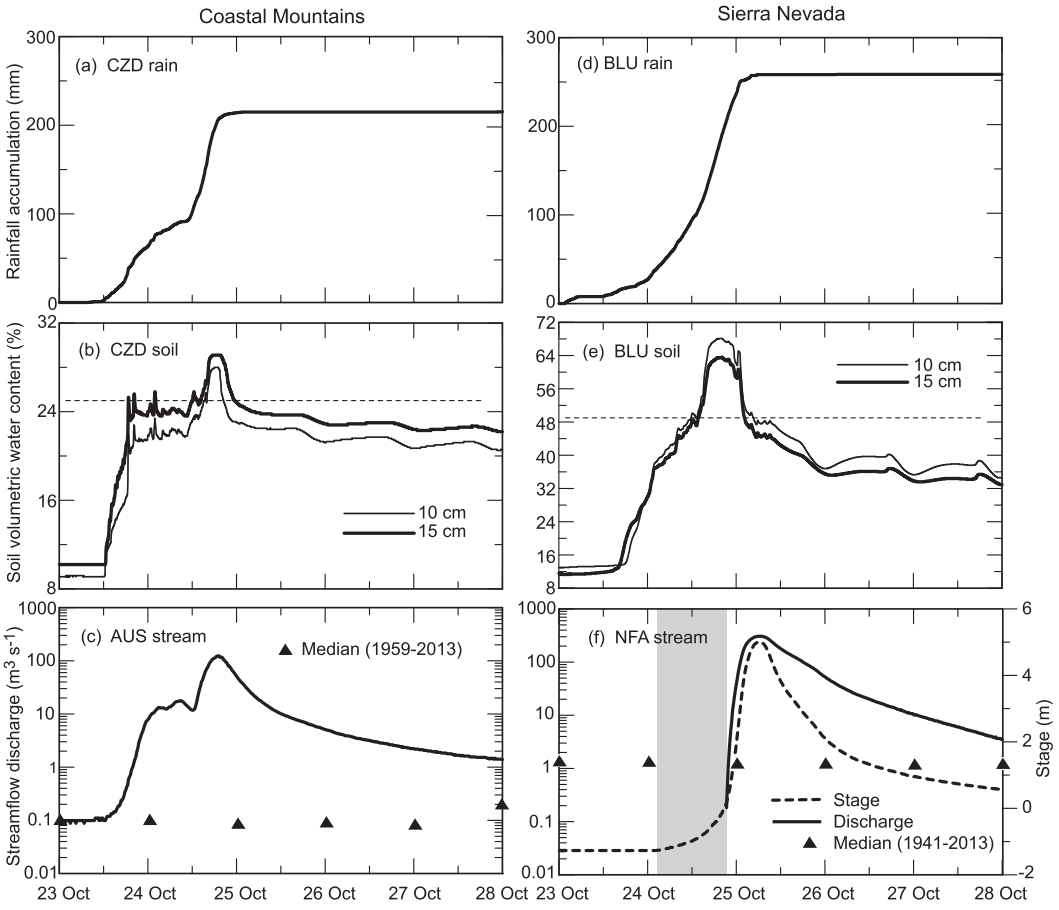

FIG. 10. Time series of observations from (left) the coastal mountains and (right) the western Sierra foothills between 0000 UTC 23 Oct and 0000 UTC 28 Oct 2010: rainfall accumulation (mm) at (a) CZD and (d) BLU; soil volumetric water content (%) at a depth of 10 and 15 cm (see key) at (b) CZD and (e) BLU, where the thin dashed horizontal lines represent soil field capacity (25% at CZD, 49% at BLU); and streamflow discharge ($m^3 s^{-1}$) at (c) AUS and (f) NFA, where triangles denote long-term daily median flows. The stage (m) at NFA is also shown. The gray-shaded bar in (f) marks the period when the reservoir stage at NFA was increasing but the water had not yet overtopped the dam (i.e., at stage = 0 m). Time increases from left to right.

draining the coastal mountains on either side of SFB attained flows in the top 5%–10% for the month of October due to increasing rainfall during the onset of AR conditions. On the two subsequent days (Figs. 11b,c), ranked flows covered much of northern California in response to the heavy rains. Orographic enhancement of precipitation within the landfalling AR yielded numerous streamflow rankings in the top 0.5%–1.0% across the coastal mountains and Sierra Nevada. Notably, the largest rankings in the top 0.1% occurred on the east side of the Sierra Nevada and quite likely reflect the transport of deep tropospheric AR water vapor across the crest, a situation that typically does not occur that early in the water year. A secondary maximum of streamflow rankings in the top 1% was situated at the north end of the CV in response to orographically enhanced rains resulting from the SBJ ascending the Shasta–Trinity region. By 26 October (Fig. 11d), the streamflow rankings ebbed across most of northern California, following the departure of the AR and the decay of the SBJ. This was a noteworthy hydrological event for the month of October, but it was a more modest event in the context of the annual cycle that includes the wet winter season. Figure 12 shows the ranking of maximum daily averaged flows for the combined 4-day window 23–26 October 2010 relative to all days observed historically between 1950 and 2012. Unlike in Fig. 11, many streamflow rankings did not exceed, or even attain, the top 5%–10%.

The warm, early season, extreme AR of October 2010 was accompanied by very high melting levels (e.g., Fig. 8) situated well above the Sierra crest (i.e., only rain fell into the mountain basins), which represents an ideal scenario for enhanced runoff and flooding during heavy rainfall (e.g., White et al. 2002; Lundquist et al. 2008).

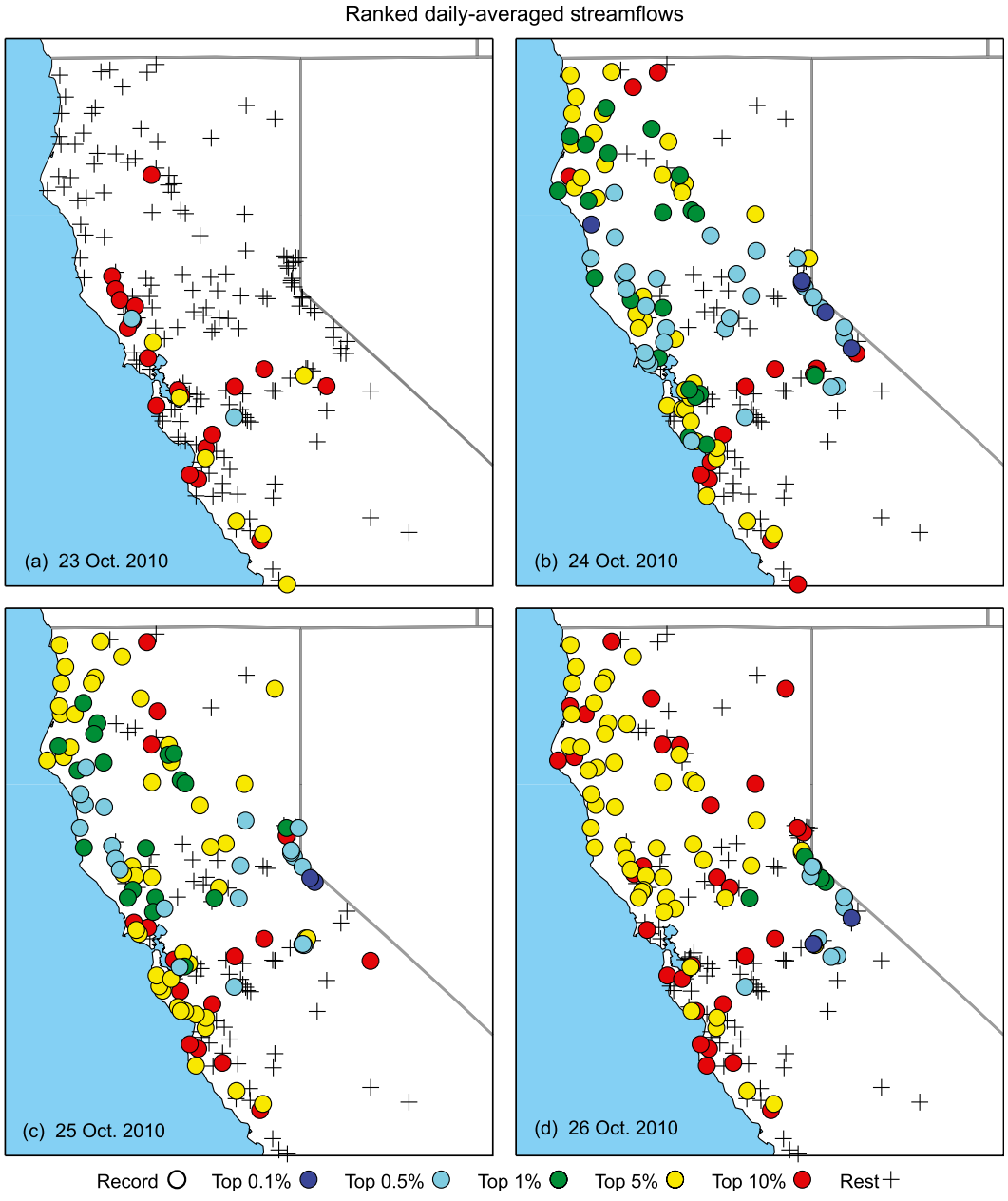

FIG. 11. Ranking of daily averaged streamflows (percentile; color-coded, see scale) relative to all available October days from October 1950 through October 2012 for (a) 23 Oct, (b) 24 Oct, (c) 25 Oct, and (d) 26 Oct 2011. These data are based on Pacific Daylight Time (add 7 h to convert to UTC). A minimum of 20 years of October data are required at each stream gauge to perform the ranked analysis. This figure was generated courtesy of Mike Dettinger at the USGS.

However, the AR produced only a modest hydrological response by winter standards because of dry antecedent soils that typify the start of each new water year in northern California. The dry soils helped absorb much of the heavy rains and mitigated the streamflow response across the region. A hydrometeorological study of 91 AR landfalls in California (Ralph et al. 2013b) quantifies the connection between antecedent soil moisture and runoff in a composite sense. That is, no matter how hard it rains during a landfalling AR in California, if the soil is dry at the onset, then major flooding will not ensue.

6. Conclusions

A 915-MHz wind profiler, a GPS receiver, and surface meteorological sites in and near California's northern

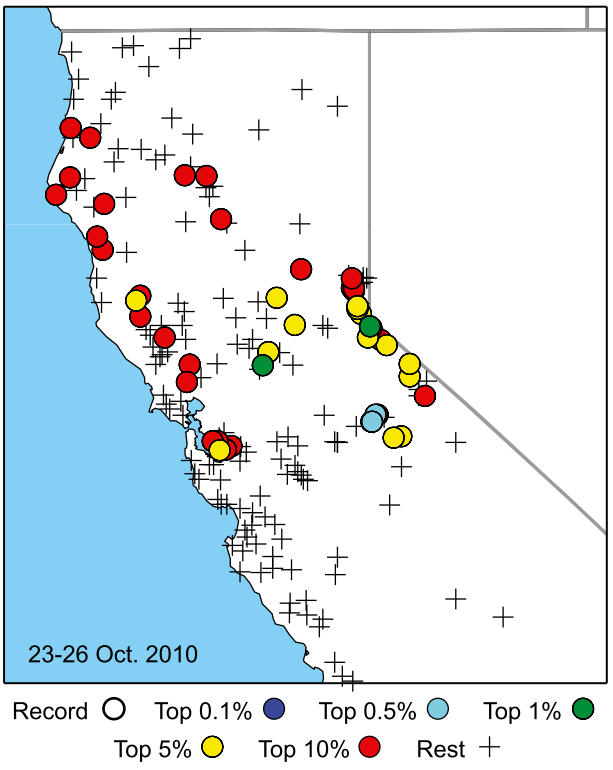

FIG. 12. Ranking of maximum daily averaged streamflows (percentile; color coded, see scale) for the 4-day period 23–26 Oct 2010 relative to all available days from 1950 through 2012. These data are based on Pacific Daylight Time (add 7 h to convert to UTC). A minimum of 20 years of data are required at each stream gauge to perform the ranked analysis. This figure was generated courtesy of Mike Dettinger at the USGS.

Central Valley provided the observational anchor for a case study that highlights key orographic impacts of an intense landfalling AR and an associated SBJ on rainfall distributions and intensities across the northern portion of the state. This event produced record early season rainfall across northern California. Flooding ensued, although it was modest in comparison to midwinter floods because of dry antecedent soil conditions (as opposed to saturated ground in winter). Regional to synoptic-scale meteorological context was provided by gridded precipitation datasets, the operational land–ocean surface network, the 32-km resolution NARR, and SSM/I satellite imagery. This study extends the early SBJ research results from SCPP (e.g., Parish 1982; Marwitz 1983, 1987; Smutz 1986) and from the recent AR–SBJ results borne out of NOAA's HMT efforts and the California Energy Commission's CalWater program (e.g., Neiman et al. 2010; Hughes et al. 2012; Kingsmill et al. 2013; Neiman et al. 2013a).

SSM/I satellite imagery and synoptic NARR analyses show the trans-Pacific extent of the AR, and its landfall across northern California, on 24 October 2010. Companion regional surface analyses during landfall document the enhanced SLP gradient and moist onshore flow in the pre-cold-frontal AR and a pressure ridge and downgradient south-southeasterly flow in the northern CV within the SBJ. A detailed wind profiler/GPS analysis at CCO documents the strong and moist southwesterly airstream of the AR overriding the shallow but strong south-southeasterly SBJ flow centered at ~750 m MSL, in accordance with the earlier case study of 14–16 February 2011 by Kingsmill et al. (2013) and with the composite AR–SBJ observational study by Neiman et al. (2013a). Our case study analysis also supports the composite results as follows: 1) the important role of the SBJ in diverting a portion of the shallow (<~1 km MSL), pre-cold-frontal, incoming water vapor within the AR poleward from the SFB gap to the northern CV and 2) the decay of shallow SBJ flow following the passage of the polar cold front aloft. Nevertheless, the case study was extreme in terms of its water vapor content, AR wind speeds, SBJ duration, and water vapor fluxes. The large IWV was likely influenced by the early season nature of the event when SSTs are warmer than in winter. These combined to produce extreme rainfall.

One of the key outcomes of this case study is that both the AR and SBJ are crucial factors in determining the amount and spatial distribution of precipitation in the northern Sierra Nevada and Shasta–Trinity region. As the AR and SBJ flow ascends the steep and tall terrain of the northern Sierra and Shasta–Trinity region, respectively, the precipitation is enhanced, thus generating copious and reliable water, either directly as runoff from rainfall or indirectly as snowmelt. Vertical profiles of linear correlation coefficient of hourly upslope water vapor flux versus hourly rain rate reveal that the altitude of maximum orographic forcing is lower for the shallow SBJ than for the deeper AR (i.e., 0.90 versus 1.15 km MSL, respectively). The case study extends lessons learned about orographic precipitation enhancement from coastal California (Neiman el al. 2002, 2009) to the interior northern Sierra and Shasta–Trinity region, which are vital for California's water supply and are also vulnerable to catastrophic flooding (e.g., Lund et al. 2007; Dettinger et al. 2011, 2012). In addition, our case study illustrates the overall representativeness of the orographic forcing mechanisms of this extreme precipitation event in the northern CV relative to the composite conditions of Neiman et al. (2013a) and the individual cases that comprise the composites when considerably less precipitation fell.

The results of this case study highlight the fact that extreme orographically enhanced precipitation in the northern Sierra Nevada and Mt. Shasta–Trinity Alps

region of California arise via the dual impacts of ARs and SBJs. Because this region is critical to California's water supply yet also poses a risk of catastrophic flooding in the state's capital of Sacramento, it is crucial to understand how a changing climate might alter this delicate benefit–hazard balance. For example, heavy precipitation events are generally expected to become more extreme (e.g., Trenberth 1999; Jain et al. 2005; Cayan et al. 2009), including those related to AR landfalls in California (Dettinger 2011). The unusually moist and strong landfalling AR studied here may represent a more typical winter scenario in a warmer climate where water vapor is more plentiful. This type of event in winter could be catastrophic, given that moist soils would facilitate quicker runoff and an existing snowpack would partially melt and provide additional water to the system. Because a changing climate will also likely bring higher snow levels during these type of storms (e.g., Knowles et al. 2006; Dettinger et al. 2009), a greater percentage of high mountain basins will receive rain rather than snow, thus further increasing the likelihood of enhanced runoff and flooding (e.g., White et al. 2002; Lundquist et al. 2008). Although water budgets in the relative coarse climate model projections for the Intermountain West have difficulty accurately portraying the highly impactful, finescale orographic precipitation processes such as those documented in this paper, better understanding of those processes is being fostered through ongoing field campaigns such as those conducted by NOAA and the California Energy Commission (e.g., the ongoing HMT and CalWater programs).

Acknowledgments. Gary Wick of NOAA/ESRL provided customized SSM/I satellite imagery. Allen White of NOAA/ESRL generated the terrain base map. Jason Cordeira of Plymouth State University carried out a ranked precipitation analysis over northern California using the NOAA/CPC gridded precipitation database. Mike Dettinger of the USGS generated the streamflow analyses in Figs. 11 and 12. Carroll Campbell of NOAA/ESRL provided composite radar imagery. Jim Adams drafted several figures. We are grateful for the comments and suggestions from Allen White of NOAA, Mimi Hughes of CIRES, Jason Cordeira of Plymouth State University, and two anonymous reviewers. Their efforts improved the scope and quality of this manuscript.

REFERENCES

Battan, L. J., 1973: *Radar Observations of the Atmosphere.* University of Chicago Press, 279 pp.

Beebe, R. G., and F. C. Bates, 1955: A mechanism for assisting in the release of convective instability. *Mon. Wea. Rev.,* **83,** 1–10, doi:10.1175/1520-0493(1955)083<0001:AMFAIT>2.0.CO;2.

Bergeron, T., 1937: On the physics of fronts. *Bull. Amer. Meteor. Soc.,* **18,** 265–275.

Browning, K. A., F. F. Hill, and C. W. Pardoe, 1974: Structure and mechanism of precipitation and the effect of orography in a wintertime warm sector. *Quart. J. Roy. Meteor. Soc.,* **100,** 309–330, doi:10.1002/qj.49710042505.

Carter, D. A., K. S. Gage, W. L. Ecklund, W. M. Angevine, P. E. Johnston, A. C. Riddle, J. S. Wilson, and C. R. Williams, 1995: Developments in UHF lower tropospheric wind profiling at NOAA's Aeronomy Laboratory. *Radio Sci.,* **30,** 977–1001, doi:10.1029/95RS00649.

Cayan, D., and Coauthors, 2009: Climate change scenarios and sea level rise estimates for California 2008 Climate Change Scenarios Assessment. California Energy Commission Rep. CEC-500-2009-014-D, 50 pp. [Available online at www.energy.ca.gov/2009publications/CEC-500-2009-014/CEC-500-2009-014-F.PDF.]

Cordeira, J. M., F. M. Ralph, and B. J. Moore, 2013: The development and evolution of two atmospheric rivers in proximity to western North Pacific tropical cyclones in October 2010. *Mon. Wea. Rev.,* **141,** 4234–4255, doi:10.1175/MWR-D-13-00019.1.

Crum, T. D., R. L. Alberty, and D. W. Burgess, 1993: Recording, archiving, and using WSR-88D data. *Bull. Amer. Meteor. Soc.,* **74,** 645–653, doi:10.1175/1520-0477(1993)074<0645:RAAUWD>2.0.CO;2.

Daly, C., P. Neilson, and D. L. Phillips, 1994: A statistical-topographic model for mapping climatological precipitation over mountainous terrain. *J. Appl. Meteor.,* **33,** 140–158, doi:10.1175/1520-0450(1994)033<0140:ASTMFM>2.0.CO;2.

Dettinger, M. D., 2004: Fifty-two years of "pineapple-express" storms across the West Coast of North America. U.S. Geological Survey, Scripps Institution of Oceanography for the California Energy Commission, PIER Project Rep. CEC-500-2005-004, 20 pp. [Available online at http://www.energy.ca.gov/2005publications/CEC-500-2005-004/CEC-500-2005-004.PDF.]

——, 2011: Climate change, atmospheric rivers and floods in California—A multimodel analysis of storm frequency and magnitude changes. *J. Amer. Water Resour. Assoc.,* **47,** 514–523, doi:10.1111/j.1752-1688.2011.00546.x.

——, K. Redmond, and D. Cayan, 2004: Winter orographic precipitation ratios in the Sierra Nevada—Large-scale atmospheric circulations and hydrologic consequences. *J. Hydrometeor.,* **5,** 1102–1116, doi:10.1175/JHM-390.1.

——, H. Hidalgo, T. Das, D. Cayan, and N. Knowles, 2009: Projections of potential flood regime changes in California. California Energy Commission Rep. CEC-500-2009-050-F, 54 pp. [Available online at http://www.energy.ca.gov/2009publications/CEC-500-2009-050/CEC-500-2009-050-F.PDF.]

——, F. M. Ralph, T. Das, P. J. Neiman, and D. Cayan, 2011: Atmospheric rivers, floods, and the water resources of California. *Water,* **3,** 455–478, doi:10.3390/w3020445.

——, and Coauthors, 2012: Design and quantification of an extreme winter storm scenario for emergency preparedness and planning exercises in California. *Nat. Hazards,* **60,** 1085–1111, doi:10.1007/s11069-011-9894-5.

Duan, J. M., and Coauthors, 1996: GPS Meteorology: Direct estimation of the absolute value of precipitable water. *J. Appl. Meteor.,* **35,** 830–838, doi:10.1175/1520-0450(1996)035<0830:GMDEOT>2.0.CO;2.

Fulton, R. A., J. P. Breidenbach, D.-J. Seo, D. A. Miller, and T. O'Bannon, 1998: The WSR-88D rainfall algorithm. *Wea. Forecasting,* **13,** 377–395, doi:10.1175/1520-0434(1998)013<0377:TWRA>2.0.CO;2.

Galewsky, J., and A. Sobel, 2005: Moist dynamics and orographic precipitation in northern and central California during the New Year's Flood of 1997. *Mon. Wea. Rev.,* **133,** 1594–1612, doi:10.1175/MWR2943.1.

Guan, B., N. Molotch, D. Waliser, E. Fetzer, and P. J. Neiman, 2010: Extreme snowfall events linked to atmospheric rivers and surface air temperature via satellite measurements. *Geophys. Res. Lett.,* **37,** L20401, doi:10.1029/2010GL044696.

Heggli, M. R., and R. M. Rauber, 1988: The characteristics and evolution of supercooled water in wintertime storms over the Sierra Nevada: A summary of microwave radiometric measurements taken during the Sierra Cooperative Pilot Project. *J. Appl. Meteor.,* **27,** 989–1015, doi:10.1175/1520-0450(1988)027<0989:TCAEOS>2.0.CO;2.

Higgins, R. W., V. B. S. Silvia, W. Shi, and J. Larson, 2007: Relationships between climate variability and fluctuations in daily precipitation over the United States. *J. Climate,* **20,** 3561–3579, doi:10.1175/JCLI4196.1.

Hillel, D., 1998: *Environmental Soil Physics.* Academic Press, 771 pp.

Hollinger, J. P., J. L. Peirce, and G. A. Poe, 1990: SSM/I instrument evaluation. *IEEE Trans. Geosci. Remote Sens.,* **28,** 781–790, doi:10.1109/36.58964.

Hughes, M., P. J. Neiman, E. Sukovich, and F. M. Ralph, 2012: Representation of the Sierra Barrier Jet in 11 years of a high-resolution dynamical reanalysis downscaling. *J. Geophys. Res.,* **117,** D18116, doi:10.1029/2012JD017869.

Jain, S., M. Hoerling, and J. Escheid, 2005: Decreasing reliability and increasing synchroneity of western North American streamflow. *J. Climate,* **18,** 613–618, doi:10.1175/JCLI-3311.1.

Kim, J., and H.-S. Kang, 2007: The impact of the Sierra Nevada on low-level winds and water vapor transport. *J. Hydrometeor.,* **8,** 790–804, doi:10.1175/JHM599.1.

——, D. E. Waliser, P. J. Neiman, B. Guan, J.-M. Ryoo, and G. A. Wick, 2012: Effects of atmospheric river landfalls on the cold season precipitation in California. *Climate Dyn.,* **38,** 411–429, doi:10.1007/s00382-010-0972-2.

Kingsmill, D. E., P. J. Neiman, B. J. Moore, M. Hughes, S. E. Yuter, and F. M. Ralph, 2013: Kinematic and thermodynamic structures of Sierra barrier jets and overrunning atmospheric rivers during a land-falling winter storm in northern California. *Mon. Wea. Rev.,* **141,** 2015–2036, doi:10.1175/MWR-D-12-00277.1.

Knowles, N., M. Dettinger, and D. Cayan, 2006: Trends in snowfall versus rainfall for the western United States. *J. Climate,* **19,** 4545–4559, doi:10.1175/JCLI3850.1.

Lin, Y., and K. E. Mitchell, 2005: The NCEP stage II/IV hourly precipitation analyses: Development and applications. *19th Conf. on Hydrology,* San Diego, CA, Amer. Meteor. Soc., 1.2. [Available online at https://ams.confex.com/ams/pdfpapers/83847.pdf.]

Lowndes, S., 1968: Forecasting large 24-h rainfall totals in the Dee and Clwyd River Authority Area from September to February. *Meteor. Mag.,* **97,** 226–235.

Lund, J. R., E. Hanak, E. Fleenor, R. Howitt, J. Mount, and P. Moyle, 2007: *Envisioning Futures for the Sacramento–San Joaquin Delta.* Public Policy Institute of California, 285 pp.

Lundquist, J. D., P. J. Neiman, B. E. Martner, A. B. White, D. J. Gottas, and F. M. Ralph, 2008: Rain versus snow in the Sierra Nevada, California: Comparing Doppler profiling radar and surface observations of melting level. *J. Hydrometeor.,* **9,** 194–211, doi:10.1175/2007JHM853.1.

——, J. R. Minder, P. J. Neiman, and E. M. Sukovich, 2010: Relationships between barrier jet heights, precipitation distributions, and streamflow in the northern Sierra Nevada. *J. Hydrometeor.,* **11,** 1141–1156, doi:10.1175/2010JHM1264.1.

Marwitz, J., 1983: The kinematics of orographic airflow during Sierra storms. *J. Atmos. Sci.,* **40,** 1218–1227, doi:10.1175/1520-0469(1983)040<1218:TKOOAD>2.0.CO;2.

——, 1987: Deep orographic storms over the Sierra Nevada. Part I: Thermodynamic and kinematic structure. *J. Atmos. Sci.,* **44,** 159–173, doi:10.1175/1520-0469(1987)044<0159:DOSOTS>2.0.CO;2.

Mattioli, V., E. R. Westwater, C. Cimini, J. S. Liljegren, B. M. Lesht, S. I. Gutman, and F. J. Schmidlin, 2007: Analysis of radiosonde and ground-based remotely sensed PWV data from the 2004 North Slope of Alaska Arctic Winter Radiometric Experiment. *J. Atmos. Oceanic Technol.,* **24,** 415–431, doi:10.1175/JTECH1982.1.

Mesinger, F., and Coauthors, 2006: North American Regional Reanalysis. *Bull. Amer. Meteor. Soc.,* **87,** 343–360, doi:10.1175/BAMS-87-3-343.

Morgan, M. C., 1999: Using piecewise potential vorticity inversion to diagnose frontogenesis. Part I: A partitioning of the **Q** vector applied to diagnosing surface frontogenesis and vertical motion. *Mon. Wea. Rev.,* **127,** 2796–2821, doi:10.1175/1520-0493(1999)127<2796:UPPVIT>2.0.CO;2.

Neiman, P. J., and M. A. Shapiro, 1989: Retrieving horizontal temperature gradients and advections from single-station wind profiler observations. *Wea. Forecasting,* **4,** 222–233, doi:10.1175/1520-0434(1989)004<0222:RHTGAA>2.0.CO;2.

——, F. M. Ralph, A. B. White, D. E. Kingsmill, and P. O. G. Persson, 2002: The statistical relationship between upslope flow and rainfall in California's coastal mountains: Observations during CALJET. *Mon. Wea. Rev.,* **130,** 1468–1492, doi:10.1175/1520-0493(2002)130<1468:TSRBUF>2.0.CO;2.

——, ——, G. A. Wick, Y.-H. Kuo, T.-K. Wee, Z. Ma, G. H. Taylor, and M. D. Dettinger, 2008a: Diagnosis of an intense atmospheric river impacting the Pacific Northwest: Storm summary and offshore vertical structure observed with COSMIC satellite retrievals. *Mon. Wea. Rev.,* **136,** 4398–4420, doi:10.1175/2008MWR2550.1.

——, ——, ——, J. Lundquist, and M. D. Dettinger, 2008b: Meteorological characteristics and overland precipitation impacts of atmospheric rivers affecting the West Coast of North America based on eight years of SSM/I satellite observations. *J. Hydrometeor.,* **9,** 22–47, doi:10.1175/2007JHM855.1.

——, A. B. White, F. M. Ralph, D. J. Gottas, and S. I. Gutman, 2009: A water vapour flux tool for precipitation forecasting. *Proc. Inst. Civ. Eng. Water Manage.,* **162,** 83–94.

——, E. M. Sukovich, F. M. Ralph, and M. Hughes, 2010: A seven-year wind profiler-based climatology of the windward barrier jet along California's northern Sierra Nevada. *Mon. Wea. Rev.,* **138,** 1206–1233, doi:10.1175/2009MWR3170.1.

——, M. Hughes, B. J. Moore, F. M. Ralph, and E. S. Sukovich, 2013a: Sierra barrier jets, atmospheric rivers, and precipitation characteristics in northern California: A composite perspective based on a network of wind profilers. *Mon. Wea. Rev.,* **141,** 4211–4233, doi:10.1175/MWR-D-13-00112.1.

——, F. M. Ralph, B. J. Moore, M. Hughes, K. M. Mahoney, J. Cordeira, and M. D. Dettinger, 2013b: The landfall and inland penetration of a flood-producing atmospheric river in Arizona. Part I: Observed synoptic-scale, orographic, and hydrometeorological characteristics. *J. Hydrometeor.,* **14,** 460–484, doi:10.1175/JHM-D-12-0101.1.

Pandey, G. R., D. R. Cayan, and K. P. Georgakakos, 1999: Precipitation structure in the Sierra Nevada of California during

winter. *J. Geophys. Res.,* **104,** 12 019–12 030, doi:10.1029/1999JD900103.

Parish, T. R., 1982: Barrier winds along the Sierra Nevada Mountains. *J. Appl. Meteor.,* **21,** 925–930, doi:10.1175/1520-0450(1982)021<0925:BWATSN>2.0.CO;2.

Ralph, F. M., and M. D. Dettinger, 2012: Historical and national perspectives on extreme West Coast precipitation associated with atmospheric rivers during December 2010. *Bull. Amer. Meteor. Soc.,* **93,** 783–790, doi:10.1175/BAMS-D-11-00188.1.

——, P. J. Neiman, and G. A. Wick, 2004: Satellite and CALJET aircraft observations of atmospheric rivers over the eastern North Pacific Ocean during the winter of 1997/98. *Mon. Wea. Rev.,* **132,** 1721–1745, doi:10.1175/1520-0493(2004)132<1721:SACAOO>2.0.CO;2.

——, and Coauthors, 2005a: Improving short term (0–48 h) cool-season quantitative precipitation forecasting: Recommendations from a USWRP workshop. *Bull. Amer. Meteor. Soc.,* **86,** 1619–1632, doi:10.1175/BAMS-86-11-1619.

——, P. J. Neiman, and R. Rotunno, 2005b: Dropsonde observations in low-level jets over the northeastern Pacific Ocean from CALJET-1998 and PACJET-2001: Mean vertical-profile and atmospheric-river characteristics. *Mon. Wea. Rev.,* **133,** 889–910, doi:10.1175/MWR2896.1.

——, ——, G. A. Wick, S. I. Gutman, M. D. Dettinger, D. R. Cayan, and A. B. White, 2006: Flooding on California's Russian River: The role of atmospheric rivers. *Geophys. Res. Lett.,* **33,** L13801, doi:10.1029/2006GL026689.

——, ——, G. N. Kiladis, K. Weickmann, and D. M. Reynolds, 2011: A multi-scale observational case study of a Pacific atmospheric river exhibiting tropical–extratropical connections and a mesoscale frontal wave. *Mon. Wea. Rev.,* **139,** 1169–1189, doi:10.1175/2010MWR3596.1.

——, and Coauthors, 2013a: The emergence of weather-focused testbeds linking research and forecasting operations. *Bull. Amer. Meteor. Soc.,* **94,** 1187–1211, doi:10.1175/BAMS-D-12-00080.1.

——, T. Coleman, P. J. Neiman, R. J. Zamora, and M. D. Dettinger, 2013b: Observed impacts of duration and seasonality of atmospheric-river landfalls on soil moisture and runoff in coastal northern California. *J. Hydrometeor.,* **14,** 443–459, doi:10.1175/JHM-D-12-076.1.

Reeves, H. D., Y.-L. Lin, and R. Rotunno, 2008: Dynamic forcing and mesoscale variability of heavy precipitation events over the Sierra Nevada Mountains. *Mon. Wea. Rev.,* **136,** 62–77, doi:10.1175/2007MWR2164.1.

Reynolds, D. W., and A. S. Dennis, 1986: A review of the Sierra Cooperative Pilot Project. *Bull. Amer. Meteor. Soc.,* **67,** 513–523, doi:10.1175/1520-0477(1986)067<0513:AROTSC>2.0.CO;2.

Saha, S., and Coauthors, 2010: The NCEP Climate Forecast System Reanalysis. *Bull. Amer. Meteor. Soc.,* **91,** 1015–1057, doi:10.1175/2010BAMS3001.1.

Schaake, J., A. Henkel, and S. Cong, 2004: Application of PRISM climatologies for hydrologic modeling and forecasting in the western U.S. *18th Conf. on Hydrology,* Seattle, WA, Amer. Meteor. Soc., 5.3. [Available online at https://ams.confex.com/ams/pdfpapers/72159.pdf.]

Smith, B. L., S. E. Yuter, P. J. Neiman, and D. E. Kingsmill, 2010: Water vapor fluxes and orographic precipitation over northern California associated with a land-falling atmospheric river. *Mon. Wea. Rev.,* **138,** 74–100, doi:10.1175/2009MWR2939.1.

Smutz, S. W., 1986: A climatology of the Sierra Nevada barrier jet. M.S. thesis, Paper AS-153, Dept. of Atmospheric Science, University of Wyoming, 108 pp.

Sodemann, H., and A. Stohl, 2013: Moisture origin and meridional transport in atmospheric rivers and their association with multiple cyclones. *Mon. Wea. Rev.,* **141,** 2850–2868, doi:10.1175/MWR-D-12-00256.1.

Stewart, R. E., J. D. Marwitz, J. C. Pace, and R. E. Carbone, 1984: Characteristics through the melting layer of stratiform clouds. *J. Atmos. Sci.,* **41,** 3227–3237, doi:10.1175/1520-0469(1984)041<3227:CTTMLO>2.0.CO;2.

Trenberth, K. E., 1999: Conceptual framework for changes of extremes of the hydrological cycle with climate change. *Climatic Change,* **42,** 327–339, doi:10.1023/A:1005488920935.

Veihmeyer, F. J., and A. H. Hendrickson, 1931: The moisture equivalent as a measure of the field capacity of soils. *Soil Sci.,* **32,** 181–193, doi:10.1097/00010694-193109000-00003.

Weber, B. L., D. B. Wuertz, D. C. Welsh, and R. McPeek, 1993: Quality controls for profiler measurements of winds and RASS temperatures. *J. Atmos. Oceanic Technol.,* **10,** 452–464, doi:10.1175/1520-0426(1993)010<0452:QCFPMO>2.0.CO;2.

Wentz, F. J., 1995: The intercomparison of 53 SSM/I water vapor algorithms. Remote Sensing Systems Tech. Rep. on WetNet Water Vapor Intercomparison Project (VIP), Santa Rosa, CA, 19 pp.

White, A. B., D. J. Gottas, E. Strem, F. M. Ralph, and P. J. Neiman, 2002: An automated bright-band height detection algorithm for use with Doppler radar vertical spectral moments. *J. Oceanic Atmos. Technol.,* **19,** 687–697, doi:10.1175/1520-0426(2002)019<0687:AABHDA>2.0.CO;2.

——, and Coauthors, 2012: NOAA's rapid response to the Howard A. Hanson Dam flood risk management crisis. *Bull. Amer. Meteor. Soc.,* **93,** 189–207, doi:10.1175/BAMS-D-11-00103.1.

Zamora, R. J., F. M. Ralph, E. Clark, and T. Schneider, 2011: The NOAA Hydrometeorology Testbed soil moisture observing networks: Design, instrumentation, and preliminary results. *J. Atmos. Oceanic Technol.,* **28,** 1129–1140, doi:10.1175/2010JTECHA1465.1.

Zhang, J., and Coauthors, 2011: National mosaic and multi-sensor QPE (NMQ) system: Description, results, and future plans. *Bull. Amer. Meteor. Soc.,* **92,** 1321–1338, doi:10.1175/2011BAMS-D-11-00047.1.

Zhu, Y., and R. E. Newell, 1998: A proposed algorithm for moisture fluxes from atmospheric rivers. *Mon. Wea. Rev.,* **126,** 725–735, doi:10.1175/1520-0493(1998)126<0725:APAFMF>2.0.CO;2.